HHS Public Access

Author manuscript

Dev Dyn. Author manuscript; available in PMC 2022 August 01.

Published in final edited form as:

Dev Dyn. 2021 August ; 250(8): 1056–1073. doi:10.1002/dvdy.312.

Genetic disruption of zebrafish *mab21l1* reveals a conserved role in eye development and affected pathways

Sarah E. Seese[1,2], **Brett Deml**[1,2,3], **Sanaa Muheisen**[1], **Elena Sorokina**[1], **Elena V. Semina**[1,2,4,5]

[1]Department of Pediatrics, The Medical College of Wisconsin, Milwaukee, Wisconsin

[2]Cell Biology, Neurobiology and Anatomy, The Medical College of Wisconsin, Milwaukee, Wisconsin

[3]PreventionGenetics, Marshfield, Wisconsin

[4]Department of Ophthalmology and Visual Sciences, Medical College of Wisconsin, Children's of Wisconsin, Milwaukee, Wisconsin

[5]Children's Research Institute, Medical College of Wisconsin, Children's of Wisconsin, Milwaukee, Wisconsin

Abstract

Background: The male-abnormal 21 like (*MAB21L*) genes are important in human ocular development. Homozygous loss of *MAB21L1* leads to corneal dystrophy in all affected individuals along with cataracts and buphthalmos in some. The molecular function and downstream pathways of MAB21L factors are largely undefined.

Results: We generated the first *mab21l1* zebrafish mutant carrying a putative loss-of-function allele, *c.107delA* p.(Lys36Argfs*7). At the final stages of embryonic development, homozygous *mab21l1*$^{c.107delA}$ fish displayed enlarged anterior chambers and corneal thinning which progressed with age. Additional studies revealed increased cell death in the mutant corneas, transformation of the cornea into a skin-like epithelium, and progressive lens degeneration with development of fibrous masses in the anterior chamber. RNA-seq of wild-type and mutant ocular transcriptomes revealed significant changes in expression of several genes, including *irf1a* and *b, stat1, elf3, krt17, tlr9*, and *loxa* associated with immunity and/or corneal function. Abnormal expression of lysyl oxidases have been previously linked with corneal thinning, fibrosis, and lens defects in

Correspondence Elena V. Semina, Department of Pediatrics, The Medical College of Wisconsin, Milwaukee, Wisconsin. esemina@mcw.edu.

AUTHOR CONTRIBUTIONS

Sarah Seese: Data curation; formal analysis; investigation; methodology; writing-original draft; writing-review & editing. **Brett Deml:** Formal analysis; investigation; methodology; validation; writing-review & editing. **Sanaa Muheisen:** Formal analysis; investigation; methodology; validation; writing-review & editing. **Elena Sorokina:** Formal analysis; investigation; methodology; writing-review & editing. **Elena Semina:** Conceptualization; methodology; project administration; resources; supervision; writing-original draft; writing-review & editing.

DISCLOSURE STATEMENT

The authors declare no conflict of interest.

SUPPORTING INFORMATION

Additional supporting information may be found online in the Supporting Information section at the end of this article.

mammals, suggesting a role for *loxa* misexpression in the progressive *mab21l1*$^{c.107delA}$ eye phenotype.

Conclusions: Zebrafish *mab21l1* is essential for normal corneal development, similar to human *MAB21L1*. The identified molecular changes in *mab21l1*$^{c.107delA}$ mutants provide the first clues about possible affected pathways.

Keywords

cataracts; corneal dystrophy; IRF1; LOX; MAB21L1; TALEN; transcriptome

1 | INTRODUCTION

The male-abnormal 21 like family has four members in humans, *MAB21L1, MAB21L2, MAB21L3*, and *MAB21L4* with their corresponding roles in development only beginning to be understood. MAB21L1 and MAB21L2 are closely related and share 94% protein identity, suggesting conserved function, whereas MAB21L3 and MAB21L4 proteins exhibit only ~25% and 20% to 22% identity with them, respectively. *MAB21L2* was the first member to be linked with human disease, as both dominant and recessive alleles in this gene were shown to cause microphthalmia, anophthalmia, and coloboma (MAC) phenotypes with skeletal defects.[1-3] More recently, two papers have reported homozygous mutations in *MAB21L1* in individuals from six unrelated families exhibiting corneal dystrophy, facial dysmorphism, scrotal agenesis and cerebellar malformation.[4,5]

The function(s) of this protein family remains largely unknown, and consequently, the molecular mechanisms contributing to the disease are not currently understood. Originally identified in *Caenorhabditis elegans, mab-21* was shown to be important for cell-fate determination, where mutations in the gene resulted in a transformation of sensory ray morphology.[6] More recently, the solved crystal structure of MAB21L1 revealed a high degree of structural similarity to inactive cyclic GMP-AMP synthase (cGAS) encoded by *MB21D1* gene and otherwise known as MAB21 domain-containing protein 1,[7] a nucleotidyltransferase (NTase) involved in the recognition of cytosolic DNA and the production of the second messenger 2′,3′-cGAMP.[8,9] However, subsequent co-crystallization with various nucleoside triphosphates only identified binding to CTP and this binding was not accompanied by any conformational change to an active state, suggesting that MAB21L1 is unlikely to have NTase capacity.[7] Consistent with this finding, MAB21L2 failed to display any enzymatic activity when challenged with ATP with measured pyrophosphate release.[3] Additionally, both MAB21L1 and MAB21L2 were found to have mild affinity for nucleic acid binding, predominantly single-stranded RNA.[3,7] Finally, a role in transcriptional regulation has been proposed, as MAB21L2 was shown to interact with SMAD complexes in response to BMP signaling and subcellular localization within the cell nuclei has been reported for both Mab21l1 and Mab21l2.[10,11]

Zebrafish (*Danio rerio*) is a well-regarded model for congenital ocular disorders due to the highly conserved developmental processes and structural anatomy with other vertebrates, including humans. One ortholog of human *MAB21L1, mab21l1* has been identified in zebrafish and the encoded protein shares 97% identity with the human ortholog. Transcript

expression of *mab21l1* has been detected throughout the embryonic ocular structures, as well as in the brain, olfactory bulbs, and branchial arches, alluding to an important role in development.[12,13]

In this publication, we describe the first genetic zebrafish model of *mab21l1*-deficiency established via TALEN-mediated genome editing technology. The presented data expands knowledge of the developmental role of *MAB21L1/mab21l1* in vertebrate species, along with the spectrum of phenotypes associated with its deficiency, with emphasis on ocular abnormalities, and suggests affected pathways.

2 | RESULTS

2.1 | Zebrafish *mab21l1* shows a robust expression during corneal and lens development and maturation

Zebrafish *mab21l1* was previously demonstrated to be expressed as early as 11-hpf in the optic vesicles and midbrain.[12,13] By 24-hpf, *mab21l1* is detected in hindbrain, tectum, olfactory bulb and the developing retina.[12,13] By 3-dpf and persisting to 5-dpf, *mab21l1* was observed in the amacrine and ganglion cell layers of the retina, in the ciliary marginal zones, along with tectum, hindbrain and branchial arches.[12] To investigate expression of *mab21l1* during the development and maturation of anterior segment structures, we performed *in situ* hybridization using eye sections at embryonic (3- and 5-dpf) and juvenile (45-dpf) stages. A robust expression was observed in the developing cornea (central and peripheral), anterior lens epithelium, iris and iridocorneal angle (Figure 1).

2.2 | *mab21l1* loss-of-function mutants have reduced survival and ocular defects

To further explore the developmental role of *mab21l1* in zebrafish, we utilized TALEN genome editing technology to generate a *mab21l1*-deficient line. Several F1 generation fish were identified with germline frameshift alleles within the *mab21l1* gene that resulted in premature stop codons, including: *mab21l1-c.107delA* p.(Lys36Argfs*7), *mab21l1-c.107_111delAGGTG* p.(Lys36Serfs*24), *mab2 1l1-c.108_109delGG* p.(Lys36Asnfs*25), and *mab21l1-c.110_111delTG* p.(Val37Glyfs*24). The *mab21l1-c.107delA* p.(Lys36Argfs*7) line was selected for further characterization (Figure 2A). Adult zebrafish heterozygous for the *mab21l1-c.107delA* p.(Lys36Argfs*7) mutant allele were crossed to generate homozygous embryos. Transcript expression in 5-dpf homozygous mutant embryos was measured using RT-PCR and RNA extracted from the larval trunks (Figure 2B). Mutant *mab21l1* transcripts were present at similar levels to wild-type with no evidence of nonsense-mediated decay (NMD), consistent with predictions since *mab21l1* is a single-exon gene, and thus considered to be insensitive to NMD. However, the protein encoded by the mutant transcript is expected to be severely truncated (at ~12% of its total length; Figure 2A) and likely targeted for degradation, thus the mutation is predicted to generate a complete loss-of-function allele.

Homozygous *mab21l1*$^{c.107delA}$ embryos were identified in 25% of the progeny of heterozygote adults consistent with Mendelian ratios. Detailed observations of the homozygous larvae at 1-5-dpf did not identify any gross morphological defects (Figure 2C-

F) except for an enlarged anterior chamber at 5-dpf (Figure 2G-I); additional measurements performed in mutant (n = 20 eyes) and wild-type (n = 16 eyes) embryos identified a statistically significant ($P = .0001$) difference in the anterior chamber area, confirming this observation. Genotyping of adult progeny of heterozygous crosses revealed 6.5% of the animals were homozygous rather than the expected 25%, suggesting reduced survival for homozygotes. Adult homozygous fish demonstrated a spectrum of ocular phenotypes (Figure 2J-Q) including misshapen/small pupils, corneal opacities, and microphthalmia, while all heterozygous fish appeared normal.

To further characterize the ocular phenotype, histological sectioning and H&E staining was performed using 3-, 5-, 8-, 10-, 14-dpf, 1 to 2 mpf and adult homozygous *mab21l1*$^{c.107delA}$ mutants (n = 9, 8, 6, 10, 15, 21, and 13 eyes, respectively) and corresponding wild-type (n = 9, 5, 4, 10, 10, 10, and 8 eyes, respectively) fish. While no difference was observed in embryos at 3-dpf (Figure 3A, B), histological analysis at later stages (5-dpf and older) identified a progressive ocular disease in all. At 5-dpf, mild thinning of some mutant corneas (Figure 3C,D) on histological sections was detected. Measurement of the central cornea thickness confirmed significantly thinner corneas in *mab21l1*$^{c.107delA}$ embryos ($P = .0048$; Figure 3O). H&E staining of mutant eyes at later stages continued to demonstrate thinner corneas, particularly at 14-dpf and 1-mpf (Figure 3E-H). Additionally, both the dorsal and ventral annular ligament and iris appeared underdeveloped at 14-dpf and 1-mpf, and abnormal persistent hyaloid vasculature was present in the posterior segment of 14-dpf mutants (Figure 3F,H). In adult *mab21l1*$^{c.107delA}$ fish, corneal layers appear distorted, with thinner epithelium and fibrous masses being present in the iridocorneal angle and between the lens and cornea (Figure 3I-L). Lens abnormalities are evident starting from 1-mpf; the lens appeared irregularly shaped and degenerative, especially in adults, as supported by both transverse and sagittal sections (Figure 3N).

2.3 | Marker analysis identifies defects in corneal development

To further characterize the ocular phenotype in mutants, wild-type and *mab21l1*$^{c.107delA}$ homozygous eye sections were analyzed using the following markers: DAPI ((4′,6-diamidino-2-phenylindole), Periodic acid-Schiff (PAS), corneal keratan sulfate proteoglycan (CKS), cadherin 2 (cdh2), and terminal deoxynucleotidyl transferase dUTP nick end labeling (TUNEL).

Staining of 5-dpf wild-type (n = 3 eyes) and homozygous *mab21l1*$^{c.107delA}$ mutant (n = 3 eyes) eyes with cdh2, CKS, and DAPI highlighted the thinning of both cornea epithelial (cdh2, DAPI) and stromal (CKS) layers in mutants (Figure 4A-C and A′-C′). This phenotype became progressively worse at 1-mpf (n = 2 wild-type and n = 7 mutant eyes) and in adults (n = 5 wild-type and n = 4 mutant eyes) (Figure 4D-I and D′-I′). In some specimens we observed CKS staining in the outermost layer of the cornea, corneal epithelium, typically unstained by CKS. This ectopic staining appears to be labeling mucin-secreting goblet cells, suggesting their aberrant presence within the central cornea. These findings are further supported by PAS staining (which identifies mucin-secreting cells[14]) of adult eye sections (wild-type n = 2 eyes; *mab21l1*$^{c.107delA}$ n = 5 eyes; Figure 4J,K and J′,K′). While in wild-type adults, goblet cells were restricted to the ocular peripheries, in

mab21l1$^{c.107delA}$ mutants, goblet cells were detected throughout the entire cornea epithelium. Additionally, disorderly cdh2 staining was detected in the abnormal lens and the anomalous fibrous masses in the anterior chamber of mutants (Figure 4G′,H′).

TUNEL staining was performed on zebrafish transverse sections from wild-type and *mab21l1*$^{c.107delA}$ mutant fish at 5-dpf (n = 5 eyes; n = 8 eyes, respectively), 10-dpf (n = 6; n = 2), 14-dpf (n = 4; n = 5), 1-mpf (n = 4; n = 7), and adults (n = 6; n = 6). At all stages, *mab21l1*$^{c.107delA}$ mutant fish exhibited an increase in TUNEL-stained cells in comparison to wild-type fish within cornea (particularly epithelial layer), with significance at 1-mpf and adult stages (Figure 4L-M and L′-M′). Specifically, at 5-dpf 6.32% ± 10.24% of cells were TUNEL+ in *mab21l1*$^{c.107delA}$ embryos, compared with 0% observed in wild-types (P = .457); at 1-mpf, 32.59% ± 2.20% of cells were TUNEL+ in *mab21l1*$^{c.107delA}$ fish compared with 6.18% ± 4.82% in wild-types (P = .0021); and for adults, 88.42% ± 15.76% were TUNEL+ in *mab21l1*$^{c.107delA}$ mutants compared with 7.56% ± 9.81% in wild-types (P = .0081).

2.4 | Electron microscopy studies further confirm corneal defects in *mab21l1*$^{c.107delA}$ mutants

To gain additional insight into the corneal phenotype, electron microscopy was performed using 14-dpf wild-type (n = 4) and homozygous mutant (n = 5) eyes (Figure 5). The corneal architecture of wild-type eyes corresponded well with published data (Figure 5A).[15-17] The corneal epithelial layer was the thickest and outermost layer of the cornea; within the central cornea, three layers of corneal epithelial cells could be detected in an organized, stratified manner. The corneal stroma was the second thickest layer and appeared of uniform thickness across the entire structure. Finally, a monolayer of endothelial cells was recognized as the innermost layer of the cornea and was notably separated from the lens capsule with anterior chamber space defining the area between.

All *mab21l1*$^{c.107delA}$ mutant eyes (n = 5) demonstrated ocular defects of varying severity (Figure 5B-F). All specimens displayed significant thinning of the epithelial and the stromal layers within the central cornea. In contrast to the three-layer central corneal epithelium in wild-type, at most two very thin epithelial layers could be identified at the thinnest portion of the mutant central cornea (Figure 5B). In two out of five specimens the phenotype was more severe. Signs of increased cell death were observed, including the presence of multiple cells being sloughed from the outermost layer (Figure 5C). Furthermore, goblet and other cells (possibly rodlet cells) were identified in mutant corneas, characteristic of the conjunctival/skin epithelium (goblet) and diseased/wounded tissue (rodlet)[18] and not present in normal corneas (Figure 5E,F). In addition to these observations, we used EM images to measure the thickness of the corneal epithelial and stromal layers in wild-type and *mab21l1*$^{c.107delA}$ mutants in both the peripheral and central corneal regions and found a significantly thinner central epithelium (P = .00012) and central stroma (P = .0018) in the mutants, while peripheral measurements were similar (Figure 5G).

2.5 | Analysis of differentially expressed transcripts in *mab21l1*$^{c.107delA}$ eyes

To identify transcripts and pathways affected by *mab21l1* deficiency, RNA samples extracted from 5-dpf wild-type and homozygous mutant eyes were analyzed by RNA-Seq. To evaluate the variability of the total data, multidimensional scaling (MDS) analysis was performed and utilized each sample's normalized expression value (Figure 6A); this analysis demonstrated that the main source of variation was attributed to mutant vs. wild-type state with no outlier samples detected. A total of 1476 differentially expressed transcripts were identified with a fold change ≤ −2 or ≥ 2 (737 were down-regulated and 739 were up-regulated) and 648 with a fold change ≤ −3 or ≥ 3 (337 down-regulated and 311 up-regulated) (Figure 6B; Table S1).

Transcripts with a fold change of ≤ −3 or ≥ 3, were further annotated with human orthologs and homologs. Identified human orthologs/homologs were further analyzed using Ingenuity Pathway Analysis (IPA), Enrichr and The database for annotation, visualization, and integrated discovery (DAVID) to reveal enriched pathways and/or functional groups. This analysis predicted numerous enhanced pathways, however, a significant overlap in gene membership between the identified groups was notable (Table S2). All three programs identified apoptosis, gap junction signaling/cell adhesion, and immunity related (Interferon Signaling, C-type lectin receptor signaling) pathways as significantly affected. Additional pathways included Sphingosine-1-phosphate and death receptor signaling (IPA), Necroptosis and NOD-like Receptor Signaling (Enrichr), Lens Development, Visual Perception and Positive Regulation of Transcription (DAVID). The predicted enrichment of factors associated with apoptosis, necroptosis and ferroptosis in differentially expressed genes is consistent with the observed increase in cell death in *mab21l1*$^{c.107delA}$ homozygous embryos (Figure 4).

Since *mab21l1* is predicted to have a regulatory role, we focused our analysis on the most affected transcription factors, with a fold change of ≤ −3 or ≥ 3. This examination identified 27 transcripts, 13 down-regulated and 14 up-regulated (Figure 6C). The most significantly down-regulated transcription factor was interferon regulatory factor 1 *irf1a* (fold-change −11.27) followed by E74 like ETS transcription factor 3 *elf3* (fold-change −4.6) and signal transducer and activator of transcription 1 *stat1* (fold-change −4.28). Interestingly, mammalian *Irf1, Elf3*, and *Stat1* were previously shown to be co-regulated and/or be involved in the same pathway[19-26] as well as demonstrate corneal expression and function in corneal differentiation, healing, and immunity (biogps.org). [27-33] Evaluation of other differentially expressed transcripts identified several additional members of the IRF1 pathway with previously reported function in eye/corneal development, including *krt17* (down-regulated, fold-change −3.85), lysyl oxidase *loxa* (up-regulated, fold-change 2.14) and toll like receptor 9, *tlr9* (up-regulated, fold-change 18.87).[34-51]

Among up-regulated transcription factors, developing brain homeobox protein 2 *dbx2* (fold-change 19.6) was the most up-regulated, followed by several other genes including prospero homeobox 2 *prox2* (fold-change 5.4), heat shock transcription factor 4 *hsf4* (fold-change 5.02), members of sry-type HMG box (*sox1a* and *b* (fold-changes 3.25 and 5.2, respectively), *sox21b* (fold-change 5.03)), and sal-like families (*sall1b* [fold-change 3.1] and *sall4* [fold-change 5.06]). The majority of the up-regulated transcription factors are strongly

expressed in the developing lens (*sox1a* and *b*,[52] *sox21b*,[53] *Sall1*,[54] *Sall4/sall4*,[55,56] *prox2*,[57] *hsf4*),[58] with some retinal expression also, reported (*Dbx2* (biogps.org), *Sox1*[59,60]; *Sall1*[61]). Consistent with the up-regulation of lens transcription factors, we observed an increase in expression of genes encoding lens-specific structural proteins such as, for example, crystallins (Table S1), indicating a possible premature lens fiber differentiation defect in *mab21l1*$^{c.107delA}$ fish. Of note, *foxe3*, a lens-specific transcription factor previously reported to be down-regulated in *Mab21l1*-deficient mouse lens placode and thus suggested to serve as a downstream target of Mab21l1,[62] was also found to be significantly up-regulated in *mab21l1* zebrafish mutants (fold-change 2.76). This suggests that the control of Mab21l1/mab21l1 downstream targets may be more complex and vary between different vertebrates.

Differential expression of multiple identified transcripts was verified by qRT-PCR with the following results: *irf1a* fold-change −21.83, $P < .000001$; *stat1b* fold-change −3.29, $P = .00004$; *elf3* fold-change −3.35, $P = .0005$; *krt17* fold-change −13.72, $P < .000001$; *dbx2* fold-change 5.51, $P < .000001$; *sox21b* fold-change 5.49, $P = .000001$; *loxa* fold-change 3.36, $P = .0003$ and *tlr9* fold-change 4.63, $P = .001$. *irf1b*, a second ortholog of human *IRF1* in zebrafish, was also examined by qRT-PCR and found to be significantly down-regulated (fold-change −2.15, $P = .0007$), though to a lesser degree than *irf1a* (Figure 6D). To evaluate transcript expression at an earlier stage, qRT-PCR analysis was repeated in RNA extracted from whole eyes of 3-dpf wild-type and homozygous *mab21l1*$^{c.107delA}$ embryos (Figure 6D) with the following results: *irf1a, irf1b, stat1b*, and *krt17* were all significantly down-regulated (fold-change −1.76, −2.0, −1.66, and −10.18 and $P = .016$, .0025, .026, and < .000001, respectively) similar to 5-dpf, although to a lesser degree. *elf3* showed a trend toward a decreased expression in 3-dpf *mab21l1*$^{c.107delA}$ eyes but the difference was not significant (fold-change −1.26, $P = .395$). *tlr9* was significantly up-regulated in *mab21l1*$^{c.107delA}$ (fold-change 3.65, $P = .049$), while the other transcripts which were up-regulated at 5-dpf were found to be down-regulated or unchanged at 3-dpf, including *dbx2* (fold-change 1.94, $P = .00061$), *sox21b* (fold-change-1.35, $P = .23$) and *loxa* (fold-change −2.19, *P*-value = .0031).

3 | DISCUSSION

In this study, we present evidence of a conserved role for *MAB21L1* in vertebrate development, as demonstrated through generation of loss-of-function alleles in zebrafish and subsequent phenotypic characterization of the mutants. In humans, six unique homozygous *MAB21L1* variants have been reported; five are predicted to be loss-of-function truncation variants (p.(Cys246Leufs*18), p. (Glu281Aspfs*20), p.(Arg287Glufs*14), p.(Tyr280*) and p. (Ser93Serfs*48)) and one is a missense variant (p. [Gln233Pro]).[4,5] All patients present with similar characteristics, including ocular abnormalities, facial dysmorphisms, cerebellar hypoplasia and scrotal agenesis.[4,5] The ocular phenotype includes corneal opacities/dystrophy in all patients, as well as nystagmus, strabismus, dry eye, mild optic atrophy, buphthalmos, and cataracts in some [4,5].

The zebrafish *mab21l1*$^{c.107delA}$ homozygous mutants demonstrate corneal abnormalities at later stages of embryonic development (5-dpf). Further analysis showed that embryonic and adult mutant corneal cells, particularly epithelial layer, undergo higher rates of cell death, as

revealed by electron microscopy and TUNEL assays. This suggests a possible role for *mab21l1* in maintenance and survival of differentiated corneal cells. Analysis of misregulated genes identified through IPA, Enrichr and DAVID revealed several factors associated with p53-dependent apoptosis signaling, including *CASP7*,[63,64] *HTRA2*,[63] *TUBA3C*,[65] *CTSH*,[66] *CTSV*,[66] and *BIRC7*.[67] At the same time, misexpression of genes associated with other mechanisms of cell death, including necroptosis, which triggers an inflammatory response,[68,69] and ferroptosis, which has been shown to be involved in disease pathogenesis in several organs,[70] was also noted. Therefore, a specific cause of cell death in the *mab21l1* mutants is currently unknown and requires further studies. TUNEL staining itself is not specific for apoptosis, as DNA fragmentation can present in other forms of cellular death, and therefore additional methodologies will need to be utilized to distinguish between different mechanisms.[71]

At later stages, mutant corneal epithelium shows skin-like epithelial cell characteristics, as indicated by the presence of mucin-secreting goblet cells via CKS and PAS staining. In addition, irregularly shaped and degenerative lenses and fibrous masses in the anterior chamber space between the lens and cornea are notable in older fish. Thus, the zebrafish phenotype associated with the loss-of-function of *mab21l1* overlaps ocular features observed in human patients with homozygous loss-of-function mutations; similarly, heterozygous *mab21l1*$^{c.107delA}$ zebrafish and individuals with heterozygous *MAB21L1* loss-of-function alleles show no visible phenotype. Interestingly, *Mab21l1* null mouse displays a significantly more severe ocular phenotype[62,72]; beginning at early embryonic stages, these mutants show defects in optic cup formation and lens placode induction, leading to aphakia and severe malformation of all other eye structures.[62] Thus, the ocular phenotype observed in *mab21l1*$^{c.107delA}$ homozygous zebrafish is more limited and consistent with the related human disease. Furthermore, the phenotype in *mab21l1* mutants is unique and separate from *mab21l2*, its close homolog. Even though *mab21l2*-deficient lines, *mab21l2*^{au10} and *mab21l2*^{Q48Sfs*5}, demonstrate corneal abnormalities, such as thickening and bulging, they develop following a severe retinal and lens disorganization, similar to *Mab21l1*$^{-/-}$ mice.[1,73,74]

In order to gain the first insights into disease mechanisms, RNA-Seq and qRT-PCR analyses were performed and revealed dramatic molecular changes in the developing *mab21l1*-deficient eyes prior to (3-dpf) and at the time (5-dpf) of phenotypic onset. Mammalian orthologs of the top down-regulated transcription factors at 3- and 5-dpf (*irf1a* and *b, stat1, elf3* have strong corneal expression and a role in corneal differentiation, healing, and immunity (biogps.org). [19-33] Both *Irf1* and *Elf3* have been shown to be highly expressed in mouse cornea in both early development and adulthood,[28] with co-expression (and possible co-regulation) noted specifically in the corneal epithelium.[25] For *Elf3*, primary expression in human cell culture and mice has been noted in the terminally differentiated corneal epithelium, though conjunctival expression was also detected in mice.[33] Mammalian orthologs of another differentially expressed regulator, STAT1/Stat1, likewise have a connection with IRF1. IRF1 has been shown to be important in activating STAT1 and promoting its binding to downstream transcriptional targets[26]; STAT1 binding of GAS promoter elements has also been shown to induce *IRF1* expression itself.[20,23,24] Studies have also identified multiple genes that require both IRF1 and STAT1 to initiate

transcription[21,22] and are thought they form complexes together.[19,20] Further, *Stat1* is expressed in the cornea and other ocular tissues and has a role in keratocyte apoptosis in response to corneal epithelial injury.[27] A significant down-regulation of *irf1a* and *b, elf3*, and *stat1* transcripts in *mab21l1*$^{c.107delA}$ mutant eyes suggests a role for *mab21l1* in their regulation.

Examination of differentially expressed transcripts for genes previously associated with the above transcription factors identified *krt17, loxa*, and *tlr9*. Keratin K17 expression has been shown to be induced through the STAT1-dependent mechanisms.[40,48] A role for *KRT17* in corneal function has recently begun to be elucidated. Keratin K17 is constitutively expressed in the limbus and bulbar conjunctiva and it is up-regulated in activated keratinocytes, the major cell type participating in tissue repair during corneal wound healing.[38,42] Recently, through RNA-Seq analysis of mouse slow-cycling limbal corneal stem cells, in comparison to epidermal hair-follicle stem cells, *KRT17/Krt17* was identified as a potential limbal stem cell marker,[45] and found to be expressed in limbal induced pluripotent stem cells.[44] Human ortholog of one of the most up-regulated transcripts, TLR9, has also been connected with the IRF1 pathway; previous work has shown TLR9 ligand-binding can recruit IRF1 to the MyD88 adaptor, leading to the activation of IRF1 which will then induce expression of interferon beta.[37,46] Interestingly, patients with the corneal disease keratitis have shown an up-regulation of TLR's, including TLR9, in corneal scrape samples,[39] and several variants have been identified in TLRs in individuals affected by keratitis.[41]

Another interesting finding was the differential expression of zebrafish *loxa*, an ortholog of human *LOX*, encoding lysyl oxidase, whose expression is known to be directly induced by IRF1 via an IRF1 response element.[36,49,50] Consistent with the down-regulation of *irfla* and *b, loxa* was found to be significantly down-regulated at 3-dpf, prior to ocular phenotype detection in *mab21l1*$^{c.107delA}$ mutants. However, at 5-dpf, when corneal thinning becomes visible, *loxa* was found to be significantly up-regulated. In addition to human LOX, with which is shares 69% protein identity, zebrafish *loxa* shows high similarity with another similar enzyme, lysyl oxidase like 1, *LOXL1* (55% identity) (of note, the zebrafish orthologue of human *LOXL1, loxl1*, also has 55% identity with the human protein). Both *LOX* and *LOXL1* are linked with human eye conditions. Several genetic variants within the *LOX* gene have been associated with keratoconus, a condition characterized by progressive thinning of the cornea[34,35,51]; the degree of reduction of LOX transcript/protein was found to positively correlate with disease severity.[47] Because the functional role of LOX involves the cross-linking of collagens and elastins, it has been suggested that the reduction of this protein subsequently effects the cross-linking of collagen fibers within the corneal stroma, resulting in a weakening of the cornea.[35] The second lysyl oxidase, *LOXL1*, has been associated with exfoliation syndrome which includes deposition of abnormal fibrillar extracellular material in the anterior segment, cataracts, secondary glaucoma and other eye defects.[75,76] In mice, both deficiency and overexpression of *Loxl1* were shown to cause eye defects. *Loxl1* null mice exhibit features of exfoliation syndrome, including risk of cataract formation[77] while overexpression of *Loxl1* cDNA in transgenic mice results in lens abnormalities, insoluble protein aggregates in the posterior lens capsule, and increased intraocular pressure.[78,79]

The primary ocular phenotype noted in homozygous *mab21l1*$^{c.107delA}$ zebrafish is corneal thinning; at later stages, the development of fibrotic masses in the anterior segment, transformation of corneal epithelium into skin-like epidermis, and lens degeneration are also observed. One possible explanation for this phenotype is that the initial corneal thinning may be associated with the down-regulation of *loxa*, however, the later overexpression of *loxa* may be equally damaging to the developing eye, similar to the consequences of *Loxl1* overexpression in mice, and promote the progressive changes that are observed in the *mab21l1*$^{c.107delA}$ homozygous eyes.

The identified link between *mab21l1* and *irf1/stat1* pathway is intriguing due to a known connection between cGAS (aka MAB21 domain-containing protein 1) and immunity, including STAT1/IRF1 regulation. Analysis of the solved crystal structure of MAB21L1 identified a high amount of structural conservation with the inactive form of cGAS.[7] cGAS is a known cytosolic DNA sensor that acts through STING and IRF3 to induce expression of type I interferons,[80] which in turn can activate *IRF1*.[81] There are several other known cytosolic DNA sensors; Ku70 is responsible for recognition of longer DNA sequences and activates IRF1 (as well as IRF7) to trigger expression of type III interferon.[80,82] Based on the observed expression changes in *mab21l1*$^{c.107delA}$ mutants, we could speculate a possible role for MAB21L1 in IRF and STAT regulation. However, a mechanism of this action is unclear since, unlike cGAS, MAB21L1 is predicted to lack NTase activity.[7] Further studies will reveal how MAB21L1/mab21l1 regulates the affected pathways and which downstream genes/pathways are most critically connected with the observed corneal thinning and other progressive ocular changes in the *mab21l1*$^{c.107delA}$ mutants.

4 | EXPERIMENTAL PROCEDURES

4.1 | Animal care

All animal care and use has been approved by the Institutional Animal Care and Use Committee at the Medical College of Wisconsin. Zebrafish (*Danio rerio*) breeding and housing was performed as previously described.[83] Embryos were collected and maintained at 28°C in either E2 embryo medium or 1X phenylthiourea (PTU) to inhibit the development of pigmentation. Developmental stages were determined based on time in hours (hours post fertilization, hpf), days (days post fertilization, dpf), or months (months post fertilization, mpf) as well as morphological assessment.[84]

4.2 | RNA studies in zebrafish

To detail expression pattern of *mab21l1*, RNA-scope procedures, as previously described,[85] with modification for paraffin sections, were performed. For RNA-scope on paraffin embedded sections, manufacturer protocols for the RNAscope Multiplex Fluorescent Reagent kit V2 Assay (323 100, Advanced Cell Diagnostics) were followed including sample preparation and pretreatment, with minor modifications. The 4 μm sections were de-paraffinized, boiled for 8 minutes in Pretreat 2 followed by 15 minutes incubation with Protease Plus at 40° C before hybridization with RNAscope Probe- Dr-mab21l1 (499 621, Advanced Cell Diagnostics, Newark, California).

To compare transcript levels of *mab21l1* between wild-type and homozygous *mab21l1-c.107delA* p. (Lys36Argfs*7) zebrafish, 10 embryos at 5-dpf were collected in 1X Ringer's solution (116 mM NaCl, 2.9 mM KCl, 1.8 mM $CaCl_2 \cdot 2H_20$, 5 mM HEPES, pH 7.2) and transferred to TRI Reagent (R2050-1-200, ZymoResearch, Irvine, California) for RNA isolation. Tissue samples were homogenized at room temperature and proceeded to RNA purification using a Direct-zol RNA MiniPrep kit (R2052, ZymoResearch). Total RNA concentration and purity was measured using a NanoDrop 1000 Spectrophotometer (ThermoFisher Scientific, Waltham, Massachusetts). cDNA was synthesized from 420 ng of purified RNA using SuperScript III First Strand Synthesis System (18 080 051, ThermoFisher Scientific). Because *mab21l1* is a one exon gene, RNA was treated with Invitrogen DNase I, Amplification Grade (18 068 015, ThermoFisher Scientific) prior to cDNA synthesis and a reverse transcriptase negative control included to confirm absence of DNA contamination in samples. Zebrafish *mab21l1* and *actb1* (acting as a loading control) were amplified from cDNA using the following primers: *mab21l1*- F-5′-TACAACCCGGATCTCTGTCC-3′, R-5′-AGCCGTGATGAACTCTACCC-3′ (product size base pairs 381 [bp]); *actb1*- F-5′-GAGAAGATCTGGCATCACAC-3′, R-5′-ATCAGGTAGTCTGTCAGGTC-3′ (product size 323 bp). PCR products were analyzed via gel electrophoresis.

For whole-transcriptome analyses between wild-type and *mab21l1* mutant embryos, whole eyes of 5-dpf wild-type and homozygous *mab21l1-c.107delA* p.(Lys36Argfs*7) 5-dpf zebrafish embryos were collected in 1X Ringer's solution (50 eyes per sample, three samples per genotype). For RNA extraction and purification from samples, Ringer's solution was removed and replaced with TRI Reagent (R2050-1-200, ZymoResearch) and the Direct-zol RNA MiniPrep kit (R2052, ZymoResearch) protocol followed. RNA quality and concentration were pre-assessed using the NanoDrop 1000 Spectrophotometer (ThermoFisher Scientific). Samples were then submitted to Macrogen (Macrogen USA, Rockville, Maryland) for RNA Sequencing. Quantity and integrity of RNA was measured using the Ribogreen (#R11490, ThermoFisher) method using Victor X2 fluorometry and an Agilent Technologies (Santa Clara, California) 2100 Bioanalyzer or Tapestation. RNA integrity number (RIN) was measured and required to be greater than or equal to 7 to pass quality control (WT samples- 9.4, 8.4, 8.8; homozygous $mab21l1^{c.107delA}$ samples- 9.2, 8.8, 8.7). RNA sequencing (RNA-Seq) was conducted as previously described[86] using an Illumina Platform Sequencer and TruSeq stranded mRNA library. Macrogen also completed data analyses, including read mapping and assembly, as well as data transformation and normalization on a log2 scale and statistical analyses including calculation of fold change, nbinomWaldTest using DESeq2 and hierarchical clustering (significant results are selected based on a |fc| > =2 and *P*-value<.05). Significant differentially expressed zebrafish transcripts were annotated with homologous human transcripts as previously described.[15] Briefly, Ensembl BioMart (http://useast.ensembl.org/biomart) was used in an initial analysis, which annotated ~50% of all transcripts. The remaining transcripts were manually annotated by searching Ensembl (http://grch37.ensembl.org/Danio_rerio) for orthologues or by conducting a NCBI Standard Protein Blast (https://blast.ncbi.nlm.nih.gov) to identify a top human homolog. Human homologs were used to identify enriched affected pathways using Ingenuity Pathway Analysis (IPA) (Qiagen, Hilden, Germany), Enrichr (http://

amp.pharm.mssm.edu/Enrichr/) and The DAVID (https://david.ncifcrf.gov/home.jsp). The full RNAseq data are available from ArrayExpress database at EMBL-EBI (Accession number E-MTAB-10068).

RNA-Seq results were validated by qRT-PCR. Primers to the following transcripts were generated: *irf1a*- F-5′-CGTCTGCTGGACTGATGAAG-3′, R-5′-ATGTGGAGTTGGGTCTCCAG-3′ (product size 177 base pairs [bp]); *irf1b*- F-5′-GGACAGCGAAGCCATCTTAG-3′, R-5′-TTCGAGCTCCTCTCCTGAAC-3′ (product size 160 bp); *stat1b*- F-5′-ACTGCAGAACTGGTTCACGG-3′, R-5′-AGATTTAGCGGGTCGTTGCT-3′ (product size 114 bp); *elf3*- F-5′-CTGACCCTGAATACTCGGAGA-3′, R-5′-TTGCTTTTCTTGGACTGAATGA-3′ (product size 151 bp); *dbx2*- F-5′-GACGCAGGTGAAGATCTGGT-3′, R-5′-TGCTGATCTCCTTCTCTCTGGA-3′ (product size 71 bp); *sox21b*- F-5′-TCAATGTCCGCAAACCCGTA-3′, R-5′-AACCCAATGGTGAGGCGTAG-3′ (product size 94 bp); *krt17*- F-5′-CATCTTCGTGGTGATCTGGA-3′, R-5′-TGTGGTGGAGGTTTTGCTTG-3′ (product size 153 bp); *loxa*- F-5′-GACCCGGACAACCCATATTA-3′, R-5′-AGGTTGTACATCGGGACTCG-3′ (product size 170 bp); *tlr9*- F-5′-TCCGTCTCACAGGACTGGAT-3′, R-5′-GCCCACCGGGAATGAAAGTA-3′ (product size 177 bp). Primers were designed to either be intron flanking or spanning, when possible, to minimize DNA amplification. cDNA synthesis was performed using RNA extracted from 3 and 5-dpf embryonic eyes and the SuperScript III First Strand Synthesis system (18 080 051, ThermoFisher Scientific), as described above. For qRT-PCR experiment design, all samples were run in triplicate and a no template control included. Samples were normalized to *actb1*- F-5′-GAGAAGATCTGGCATCACAC-3′, R-5′-ATCAGGTAGTCTGTCAGGTC-3′ (product size 323 bp). Fold change was calculated for three independent biological repeats and averaged. Graphs were generated using GraphPad Prism 9 (San Diego, California; https://www.graphpad.com/scientific-software/prism/). Statistical significance was determined using an unpaired sample *t* test with a *P*-value of <.05. Heatmap was obtained by utilizing normalized values for each wild-type and homozygous *mab21l1*$^{c.107delA}$ biological sample per transcript and transforming to a row z-score. Then, conditional formatting was performed in Microsoft Excel to generate the colored table.

4.3 | Generation of *mab21l1* mutant line

Transcription activator-like effector nucleases (TALENs) were used to generate *mab21l1* deficient lines. Briefly, TALENs were designed using the Scoring Algorithm for Predicting TALEN Activity (SAPTA) program[87] to target the N-terminal region of the *mab21l1* gene with the following TALENs chosen for use: left TALEN-5′-CTCCAAGACCATCCGGGAG-3′, right TALEN-5′-CCACCTCTTTTAGGACATC-3′. TALE assembly was conducted as previously described[88] using the TALE Toolbox kit (#1000000019, Addgene, Cambridge, Massachusetts). Plasmids identified with correctly assembled TALE sequences were utilized for mRNA synthesis. Plasmids were linearized using restriction enzyme SmaI (R0141S, New England BioLabs, Ipswich, Massachusetts) and mRNA synthesized from the linearized plasmid using the Invitrogen mMESSAGE mMACHINE T7 Transcription Kit (AM1344, ThermoFisher Scientific) and the Invitrogen

Poly(A) Tailing Kit (AM1350, ThermoFisher Scientific). Zebrafish wild-type embryos were then injected at the 1 to 4 cell stage with 150 pg TALEN mRNA (75 pg of left and right TALEN, each). Injections were performed using a Drummond Nanoject II instrument (Drummond Scientific, Broomall, Pennsylvania). Genome editing events were confirmed in an initial analysis of injected embryos via BsaI restriction digestion (GGTCTC), as the TALEN targeted spacer region was predicted to uniquely contain a BsaI restriction site. To do so, genomic DNA was isolated from embryos via previously established protocols.[89] Briefly, embryos were incubated with 20 μL of 50 mM NaOH at 95°C for 20 minutes, then 2 μL of 1 M Tris-HCl pH 8.0 was added to the sample and vortexed. The *mab21l1* targeted region of interest was amplified from genomic DNA using primers F-5′-TACAACCCGGATCTCTGTCC-3′ and R-5′-AGCCGTGATGAACTCTACCC-3′ and the PCR-amplified product subsequently digested with BsaI (R3535S, New England BioLabs) and later confirmed with Sanger sequencing. Injected embryos were then raised to adulthood to establish a population of mosaic founders. These fish were in-crossed to produce offspring with germline *mab21l1* mutations (F1 generation), and the offspring subsequently raised to adulthood and genotyped as described above. Those with identifiable heterozygous mutations were bred to generate either homozygous or compound heterozygous embryos. One line, *mab21l1-c.107delA* p.(Lys36Argfs*7), was selected for further characterization.

4.4 | Microscopy and histological studies

Whole-mount images were captured of zebrafish anesthetized in 1X tricaine using a Nikon SMZ1500 dissection scope (Nikon Instruments Inc., Melville, New York) and a ZEISS SteREO Discovery.V12 microscope (Carl Zeiss Inc., Thornwood, New York) with a ZEISS AxioCam MRc (Carl Zeiss Inc.). Anterior chamber measurements of the eye were taken using dorsal images from 5-dpf wild-type and homozygous *mab21l1-c.107delA* p.(Lys36Argfs*7) embryos with Image J software (https://imagej.nih.gov/ij/index.html). To do so, the area of the anterior chamber was measured by outlining along the surface of the cornea, lens, and iris. This was normalized to the width of the eye at the widest point. Each measurement was taken three times and averaged. Graphs were generated using GraphPad Prism 9 and statistical significance was determined using an unpaired sample *t* test with a *P*-value of <.05.

For histological sections, zebrafish at 3, 5, 8, 10, 12, 14-dpf, 1-mpf, 2-mpf and 1 to 2 years of age were anesthetized in 1X tricaine and euthanized. Fish 1-mpf and younger were encapsulated in histogel (HG-4000-012, ThermoFisher Scientific) due to small specimen size. For fixation, fish were preserved in either 10% formalin or Davidson's solution (1-part glacial acetic acid, 3-parts 95% ethyl alcohol, 2-parts 10% neutral buffered formalin, and 3-parts water) and submitted to the Children's Research Institute Histology Core at the Medical College of Wisconsin for paraffin sectioning. Serial sectioning was performed in either the transverse or sagittal orientation at 4 μm thickness. Hematoxylin and eosin (H&E) staining and Periodic acid-Schiff (PAS) staining of paraffin sections were performed by the Core using standard protocols. Slides were imaged on the NanoZoomer digital slide scanner and using NDP.view 2 Viewing software (U12388-01, Hamamatsu, Hamamatsu City, Japan). Corneal thickness was measured with Image J software at 5-dpf using wild-type and homozygous *mab21l1-c.107delA* p.(Lys36Argfs*7) histological sections containing the

largest lens size. All measurements were normalized to eye diameter. Each measurement was taken three times and averaged. Results were graphed using GraphPad Prism 9 and statistical significance was determined using an unpaired sample *t* test with a *P*-value of <.05.

Electron microscopy (EM) was performed as previously described[15,16] through the Electron Microscopy Core Facility at the Medical College of Wisconsin. Briefly, 14-dpf wild-type and homozygous *mab21l1-c.107delA* p. (Lys36Argfs*7) zebrafish were anesthetized in 1X tricaine and euthanized. Fish were fixed in EM primary fixative (2% paraformaldehyde, 2.5% glutaraldehyde, 3% sucrose, 0.06% phosphate buffer pH 7.4) at 4°C. Samples were further prepared through membrane preservation in 1% osmium for 1 hour, dehydration by methanol and acetonitrile washes, and embedment in EMbed812 resin (14 120, Electron Microscopy Sciences, Hatfield, Pennsylvania). Semi-thin sections (~500 nm) were cut in a transverse manner using a PowerTome XL microtome (Boeckler Instruments, Tucson, Arizona) and DiATOME Histo Diamond Knife (HI10213, DiATOME, Hatfield, Pennsylvania) in order to properly stage the eye in the central region, roughly associated with the appearance of the ventral canal. Once appropriately positioned, ultrathin sections were collected (~70-80 nm) with the DiATOME Ultra 45° Diamond Knife (MT7376, DiATOME). Sections were mounted on a standard copper hexagonal mesh grid (G-200H-Cu, Electron Microscopy Sciences, Hatfield, Pennsylvania) and stained with uranyl acetate and lead citrate. EM images were taken on the Hitachi H600 TEM microscope (Hitachi, Tokyo, Japan). Corneal layer measurements were taken in central cornea and at corneal peripheries using ImageJ software. Each measurement was taken three times and averaged. Results were graphed using GraphPad Prism 9 and statistical significance was determined using an unpaired sample *t* test with a *P*-value of <.05.

4.5 | Immunohistochemistry and TUNEL assays

To characterize ocular phenotypes, various markers were utilized in fluorescent assays. N-cadherin (cdh2) is a well-characterized cellular adhesion protein known within the zebrafish eye to be expressed in corneal epithelium, corneal endothelium, lens epithelium, and retinal cells.[90,91] Corneal keratan sulfate proteoglycan (CKS) is a glycosaminoglycan found in high abundance within corneal stroma keratocytes in zebrafish.[17] CKS has also been previously shown to label mucin-secreting goblet cells at the ocular peripheries within conjunctiva.[15] For these experiments the following primary antibodies were used: 1:50 cdh2 (GTX125962, GeneTex, Irvine, California), 1:125 CKS (MAB2022, Millipore Sigma, Burlington, Massachusetts). The following secondary antibodies were used: 1:100 donkey anti-rabbit Alexa-Fluor 488 (A21206, ThermoFisher Scientific), 1:100 donkey anti-mouse Alexa Fluor 568 (A10037, ThermoFisher Scientific).

To visualize markers, immunohistochemistry (IHC) was performed on 5, 8, 10, 12, 14-dpf, 1-mpf, 2-mpf, and 1 to 2 year old wild-type and homozygous *mab21l1-c.107delA* p. (Lys36Argfs*7) sections. Fish were processed for paraffin sections, as described above, and sections prepared for immunohistochemistry. To unmask epitopes to allow antibody hybridization, an antigen retrieval step was included, where slides were boiled in 1X antigen retrieval solution (S169984-2, Agilent Technologies) at 100°C for 20 minutes. After, slides

were cooled at room temperature for an additional 20 minutes. This was followed by a series of washes, two 5-minute washes with water and one 10-minute wash with 1X PBT, all at room temperature. To prevent unspecific antibody interactions, slides were then blocked with 10% donkey blocking solution (DBS) and incubated in a humid chamber for 2 hours at room temperature. Then, slides were incubated with primary antibody in 10% DBS overnight at 4°C. The following day, slides were washed four times with 1X PBT, 10 minutes each at room temperature. Next, slides were incubated for 2 hours at room temperature with the appropriate secondary antibody in 10% DBS. This was followed by three washes with 1X PBT for 10 minutes at room temperature. For experiments involving double stains, slides were successively incubated with the second primary antibody, and the process repeated as described above. After the washes, slides were incubated with 1:1000 DAPI stain (D1306, ThermoFisher Scientific) for 5 minutes at room temperature. Slides were rinsed two times with 1X PBT and dried prior to coverslipping. Slides were then imaged on a ZEISS AxioImager Z1 (Carl Zeiss Inc.).

Finally, TUNEL staining was performed to identify potential differences in cell death. 5-dpf wild-type and homozygous *mab21l1-c.107delA* p.(Lys36Argfs*7) paraffin sections were used following the protocol outlined in the ApopTag Red In Situ Apoptosis Detection Kit (S7165, Millipore Sigma). In brief, slides were de-coverslipped in xylene prior to beginning experiment. Tissue was then pretreated with a proteinase K digestion (20 μg/mL) for 15 minutes at room temperature, followed by two 2-minute washes in 1X PBS. Next, 75 μL/5 cm^2 of equilibration buffer was added and incubated with the tissue for 10 minutes at room temperature. Then, any DNA fragments existing due to cellular death were labeled with digoxigenin-dNTP by adding 55 μL/5 cm^2 of TdT enzyme (working strength) and incubating for 1 hour at 37°C. The reaction was suspended by adding working strength stop/wash buffer, agitating for 15 seconds, and then incubating for 10 minutes at room temperature. The tissue sample was then washed three times with 1X PBS for 1 minute each, followed by application of 65 μL/5 cm^2 prewarmed working strength anti-digoxigenin conjugate (rhodamine) for 30 minutes in a humidified chamber at room temperature. Finally, tissue was washed four times with 1X PBS for 2 minutes per wash, and counterstained with DAPI (D1306, ThermoFisher Scientific). Tissue was then imaged via fluorescence microscopy on a ZEISS AxioImager Z1 (Carl Zeiss Inc.). For quantification, TUNEL-positive cells and DAPI stained cells were each manually counted three times on central eye sections and averaged. Percent TUNEL+/total DAPI stained cells was calculated. Results were graphed using GraphPad Prism 9 and statistical significance was determined using an unpaired sample *t* test with a *P*-value <.05.

Supplementary Material

Refer to Web version on PubMed Central for supplementary material.

ACKNOWLEDGMENTS

The authors gratefully acknowledge patients and their families for their participation in research studies. The authors also thank Linda Reis, MS, CGC, for her careful reading of the manuscript and helpful comments. Additionally, we would like to thank Christine Duris with the Children's Research Institute Histology Core, as well as Clive Wells and Robert Goodwin with the Medical College of Wisconsin Electron Microscopy Core for their knowledge and assistance with associated experiments.

Funding information

National Eye Institute, Grant/Award Numbers: R01EY025718, T32EY014537

REFERENCES

1. Deml B, Kariminejad A, Borujerdi RH, Muheisen S, Reis LM, Semina EV. Mutations in MAB21L2 result in ocular Coloboma, microcornea and cataracts. PLoS Genet. 2015;11(2):e1005002. 10.1371/journal.pgen.1005002. [PubMed: 25719200]
2. Horn D, Prescott T, Houge G, et al. A novel Oculo-skeletal syndrome with intellectual disability caused by a particular MAB21L2 mutation. Eur J Med Genet. 2015;58(8):387–391. 10.1016/j.ejmg.2015.06.003. [PubMed: 26116559]
3. Rainger J, Pehlivan D, Johansson S, et al. Monoallelic and biallelic mutations in MAB21L2 cause a spectrum of major eye malformations. Am J Hum Genet. 2014;94(6):915–923. 10.1016/j.ajhg.2014.05.005. [PubMed: 24906020]
4. Bruel AL, Masurel-Paulet A, Riviere JB, et al. Autosomal recessive truncating MAB21L1 mutation associated with a syndromic scrotal agenesis. Clin Genet. 2017;91(2):333–338. 10.1111/cge.12794. [PubMed: 27103078]
5. Rad A, Altunoglu U, Miller R, et al. MAB21L1 loss of function causes a syndromic neurodevelopmental disorder with distinctive cerebellar, ocular, craniofacial and genital features (COFG syndrome). J Med Genet. 2019;56(5):332–339. 10.1136/jmedgenet-2018-105623. [PubMed: 30487245]
6. Baird SE, Fitch DH, Kassem IA, Emmons SW. Pattern formation in the nematode epidermis: determination of the arrangement of peripheral sense organs in the *C. elegans* male tail. Development. 1991;113(2):515–526. [PubMed: 1782863]
7. de Oliveira Mann CC, Kiefersauer R, Witte G, Hopfner KP. Structural and biochemical characterization of the cell fate determining nucleotidyltransferase fold protein MAB21L1. Sci Rep. 2016;6:27498. 10.1038/srep27498. [PubMed: 27271801]
8. Ablasser A, Goldeck M, Cavlar T, et al. cGAS produces a 2′-5′-linked cyclic dinucleotide second messenger that activates STING. Nature. 2013;498(7454):380–384. 10.1038/nature12306. [PubMed: 23722158]
9. Gao P, Ascano M, Wu Y, et al. Cyclic [G(2′,5′)pA(3′,5′)p] is the metazoan second messenger produced by DNA-activated cyclic GMP-AMP synthase. Cell. 2013;153(5):1094–1107. 10.1016/j.cell.2013.04.046. [PubMed: 23647843]
10. Baldessari D, Badaloni A, Longhi R, Zappavigna V, Consalez GG. MAB21L2, a vertebrate member of the male-abnormal 21 family, modulates BMP signaling and interacts with SMAD1. BMC Cell Biol. 2004;5(1):48. 10.1186/1471-2121-5-48. [PubMed: 15613244]
11. Mariani M, Baldessari D, Francisconi S, et al. Two murine and human homologs of mab-21, a cell fate determination gene involved in *Caenorhabditis elegans* neural development. Hum Mol Genet. 1999;8(13):2397–2406. 10.1093/hmg/8.13.2397. [PubMed: 10556287]
12. Cederlund ML, Vendrell V, Morrissey ME, et al. mab21l2 transgenics reveal novel expression patterns of mab21l1 and mab21l2, and conserved promoter regulation without sequence conservation. Dev Dyn. 2011;240(4):745–754. 10.1002/dvdy.22573. [PubMed: 21360786]
13. Wong YM, Chow KL. Expression of zebrafish mab21 genes marks the differentiating eye, midbrain and neural tube. Mech Dev. 2002;113(2):149–152. 10.1016/s0925-4773(02)00012-6. [PubMed: 11960703]
14. Gage PJ, Qian M, Wu D, Rosenberg KI. The canonical Wnt signaling antagonist DKK2 is an essential effector of PITX2 function during normal eye development. Dev Biol. 2008;317(1):310–324. 10.1016/j.ydbio.2008.02.030. [PubMed: 18367164]
15. Hendee KE, Sorokina EA, Muheisen SS, et al. PITX2 deficiency and associated human disease: insights from the zebrafish model. Hum Mol Genet. 2018;27(10):1675–1695. 10.1093/hmg/ddy074. [PubMed: 29506241]
16. Soules KA, Link BA. Morphogenesis of the anterior segment in the zebrafish eye. BMC Dev Biol. 2005;5:12. 10.1186/1471-213X-5-12. [PubMed: 15985175]

17. Zhao XC, Yee RW, Norcom E, et al. The zebrafish cornea: structure and development. Invest Ophthalmol Vis Sci. 2006;47(10):4341–4348. 10.1167/iovs.05-1611. [PubMed: 17003424]
18. Reite OB. The rodlet cells of teleostean fish: their potential role in host defence in relation to the role of mast cells/eosinophilic granule cells. Fish Shellfish Immunol. 2005;19(3):253–267. 10.1016/j.fsi.2005.01.002. [PubMed: 15820126]
19. Abou El Hassan M, Huang K, Eswara MB, et al. Properties of STAT1 and IRF1 enhancers and the influence of SNPs. BMC Mol Biol. 2017;18(1):6. 10.1186/s12867-017-0084-1. [PubMed: 28274199]
20. Antonczyk A, Krist B, Sajek M, et al. Direct inhibition of IRF-dependent transcriptional regulatory mechanisms associated with disease. Front Immunol. 2019;10:1176. 10.3389/fimmu.2019.01176. [PubMed: 31178872]
21. Chatterjee-Kishore M, Wright KL, Ting JP, Stark GR. How Stat1 mediates constitutive gene expression: a complex of unphosphorylated Stat1 and IRF1 supports transcription of the LMP2 gene. EMBO J. 2000;19(15):4111–4122. 10.1093/emboj/19.15.4111. [PubMed: 10921891]
22. Ramsauer K, Farlik M, Zupkovitz G, et al. Distinct modes of action applied by transcription factors STAT1 and IRF1 to initiate transcription of the IFN-gamma-inducible gbp2 gene. Proc Natl Acad Sci U S A. 2007;104(8):2849–2854. 10.1073/pnas.0610944104. [PubMed: 17293456]
23. Schroder K, Hertzog PJ, Ravasi T, Hume DA. Interferon-gamma: an overview of signals, mechanisms and functions. J Leukoc Biol. 2004;75(2):163–189. 10.1189/jlb.0603252. [PubMed: 14525967]
24. Sikorski K, Chmielewski S, Olejnik A, et al. STAT1 as a central mediator of IFNgamma and TLR4 signal integration in vascular dysfunction. JAKSTAT. 2012;1(4):241–249. 10.4161/jkst.22469. [PubMed: 24058779]
25. Stephens DN, Klein RH, Salmans ML, Gordon W, Ho H, Andersen B. The Ets transcription factor EHF as a regulator of cornea epithelial cell identity. J Biol Chem. 2013;288(48):34304–34324. 10.1074/jbc.M113.504399. [PubMed: 24142692]
26. Zenke K, Muroi M, Tanamoto KI. IRF1 supports DNA binding of STAT1 by promoting its phosphorylation. Immunol Cell Biol. 2018;96(10):1095–1103. 10.1111/imcb.12185. [PubMed: 29893425]
27. Mohan RR, Mohan RR, Kim WJ, Stark GR, Wilson SE. Defective keratocyte apoptosis in response to epithelial injury in stat 1 null mice. Exp Eye Res. 2000;70(4):485–491. 10.1006/exer.1999.0807. [PubMed: 10865997]
28. Norman B, Davis J, Piatigorsky J. Postnatal gene expression in the normal mouse cornea by SAGE. Invest Ophthalmol Vis Sci. 2004;45(2):429–440. 10.1167/iovs.03-0449. [PubMed: 14744882]
29. Sato M, Taniguchi T, Tanaka N. The interferon system and interferon regulatory factor transcription factors - - studies from gene knockout mice. Cytokine Growth Factor Rev. 2001;12(2–3):133–142. 10.1016/s1359-6101(00)00032-0. [PubMed: 11325597]
30. Taniguchi T, Ogasawara K, Takaoka A. Tanaka N. IRF family of transcription factors as regulators of host defense. Annu Rev Immunol. 2001;19:623–655. 10.1146/annurev.immunol.19.1.623. [PubMed: 11244049]
31. Wu C, Jin X, Tsueng G, Afrasiabi C, Su AI. BioGPS: building your own mash-up of gene annotations and expression profiles. Nucleic Acids Res. 2016;44(D1):D313–D316. 10.1093/nar/gkv1104. [PubMed: 26578587]
32. Yoon GS, Dong C, Gao N, Kumar A, Standiford TJ, Yu FS. Interferon regulatory factor-1 in flagellin-induced reprogramming: potential protective role of CXCL10 in cornea innate defense against *Pseudomonas aeruginosa* infection. Invest Ophthalmol Vis Sci. 2013;54(12):7510–7521. 10.1167/iovs.13-12453. [PubMed: 24130180]
33. Yoshida N, Yoshida S, Araie M, Handa H, Nabeshima Y. Ets family transcription factor ESE-1 is expressed in corneal epithelial cells and is involved in their differentiation. Mech Dev. 2000;97(1–2):27–34. 10.1016/s0925-4773(00)00419-6. [PubMed: 11025204]
34. Bykhovskaya Y, Li X, Epifantseva I, et al. Variation in the lysyl oxidase (LOX) gene is associated with keratoconus in family-based and case-control studies. Invest Ophthalmol Vis Sci. 2012;53(7):4152–4157. 10.1167/iovs.11-9268. [PubMed: 22661479]

35. Bykhovskaya Y, Margines B, Rabinowitz YS. Genetics in Keratoconus: where are we? Eye Vis. 2016;3(16):16. 10.1186/s40662-016-0047-5.
36. Chen FF, Jiang G, Xu K, Zheng JN. Function and mechanism by which interferon regulatory factor-1 inhibits oncogenesis. Oncol Lett. 2013;5(2):417–423. 10.3892/ol.2012.1051. [PubMed: 23420765]
37. Colonna M TLR pathways and IFN-regulatory factors: to each its own. Eur J Immunol. 2007;37(2):306–309. 10.1002/eji.200637009. [PubMed: 17273997]
38. Gordon MK, Gerecke DR, Zhou P, Hahn R, Joseph LB, Chang Y. Epithelial repair in the rabbit cornea following aspects of epithelial injury and repair after mustard exposure. FASEB J. 2020;34(S1):1–1. 10.1096/fasebj.2020.34.s1.07007.
39. Karthikeyan RS, Priya JL, Leal SM Jr, et al. Host response and bacterial virulence factor expression in Pseudomonas aeruginosa and *Streptococcus pneumoniae* corneal ulcers. PLoS One. 2013;8(6):e64867. 10.1371/journal.pone.0064867. [PubMed: 23750216]
40. Komine M, Freedberg IM, Blumenberg M. Regulation of epidermal expression of keratin K17 in inflammatory skin diseases. J Invest Dermatol. 1996;107(4):569–575. 10.1111/1523-1747.ep12582820. [PubMed: 8823363]
41. Konda N, Kaur I, Garg P, Chakrabarti S, Willcox MDP. Toll-like receptor gene polymorphisms in patients with keratitis. Cont Lens Anterior Eye. 2020. 10.1016/j.clae.2020.07.003.
42. Pearton DJ, Yang Y, Dhouailly D. Transdifferentiation of corneal epithelium into epidermis occurs by means of a multistep process triggered by dermal developmental signals. Proc Natl Acad Sci U S A. 2005;102(10):3714–3719. 10.1073/pnas.0500344102. [PubMed: 15738417]
43. Rodriguez-Martinez S, Cancino-Diaz ME, Jimenez-Zamudio L, Garcia-Latorre E, Cancino-Diaz JCTLR. NODs mRNA expression pattern in healthy mouse eye. Br J Ophthalmol. 2005;89(7):904–910. 10.1136/bjo.2004.056218. [PubMed: 15965176]
44. Sareen D, Saghizadeh M, Ornelas L, et al. Differentiation of human limbal-derived induced pluripotent stem cells into limbal-like epithelium. Stem Cells Transl Med. 2014;3(9):1002–1012. 10.5966/sctm.2014-0076. [PubMed: 25069777]
45. Sartaj R, Zhang C, Wan P, et al. Characterization of slow cycling corneal limbal epithelial cells identifies putative stem cell markers. Sci Rep. 2017;7(1):3793. 10.1038/s41598-017-04006-y. [PubMed: 28630424]
46. Schmitz F, Heit A, Guggemoos S, et al. Interferon-regulatory-factor 1 controls toll-like receptor 9-mediated IFN-beta production in myeloid dendritic cells. Eur J Immunol. 2007;37(2):315–327. 10.1002/eji.200636767. [PubMed: 17273999]
47. Shetty R, Sathyanarayanamoorthy A, Ramachandra RA, et al. Attenuation of lysyl oxidase and collagen gene expression in keratoconus patient corneal epithelium corresponds to disease severity. Mol Vis. 2015;21:12–25. [PubMed: 25593510]
48. Shi X, Jin L, Dang E, et al. IL-17A upregulates keratin 17 expression in keratinocytes through STAT1- and STAT3-dependent mechanisms. J Invest Dermatol. 2011;131(12):2401–2408. 10.1038/jid.2011.222. [PubMed: 21796151]
49. Takaoka A, Tamura T, Taniguchi T. Interferon regulatory factor family of transcription factors and regulation of oncogenesis. Cancer Sci. 2008;99(3):467–478. 10.1111/j.1349-7006.2007.00720.x. [PubMed: 18190617]
50. Tan RS, Taniguchi T. Harada H identification of the lysyl oxidase gene as target of the antioncogenic transcription factor, IRF-1, and its possible role in tumor suppression. Cancer Res. 1996;56(10):2417–2421. [PubMed: 8625321]
51. Zhang J, Zhang L, Hong J, Wu D, Xu J. Association of Common Variants in LOX with Keratoconus: a meta-analysis. PLoS One. 2015;10(12):e0145815. 10.1371/journal.pone.0145815. [PubMed: 26713757]
52. Gerber V, Yang L, Takamiya M, et al. The HMG box transcription factors Sox1a and Sox1b specify a new class of glycinergic interneuron in the spinal cord of zebrafish embryos. Development. 2019;146(4). 10.1242/dev.172510.
53. Pauls S, Smith SF, Elgar G. Lens development depends on a pair of highly conserved Sox21 regulatory elements. Dev Biol. 2012;365(1):310–318. 10.1016/j.ydbio.2012.02.025. [PubMed: 22387845]

54. Baba Y, Watabe Y, Sagara H, Watanabe S. Sall1 plays pivotal roles for lens fiber cell differentiation in mouse. Biochem Biophys Res Commun. 2019;512(4):927–933. 10.1016/j.bbrc.2019.03.098. [PubMed: 30929925]
55. Jackson R, Braubach OR, Bilkey J, et al. Expression of sall4 in taste buds of zebrafish. Dev Neurobiol. 2013;73(7):543–558. 10.1002/dneu.22079. [PubMed: 23447551]
56. Ullah E, Wu D, Madireddy L, et al. Two missense mutations in SALL4 in a patient with microphthalmia, coloboma, and optic nerve hypoplasia. Ophthalmic Genet. 2017;38(4):371–375. 10.1080/13816810.2016.1217550. [PubMed: 27661448]
57. Pistocchi A, Bartesaghi S, Cotelli F, Del Giacco L. Identification and expression pattern of zebrafish prox2 during embryonic development. Dev Dyn. 2008;237(12):3916–3920. 10.1002/dvdy.21798. [PubMed: 19035352]
58. Gao M, Huang Y, Wang L, et al. HSF4 regulates lens fiber cell differentiation by activating p53 and its downstream regulators. Cell Death Dis. 2017;8(10):e3082. 10.1038/cddis.2017.478. [PubMed: 28981088]
59. Ishii Y, Weinberg K, Oda-Ishii I, Coughlin L, Mikawa T. Morphogenesis and cytodifferentiation of the avian retinal pigmented epithelium require downregulation of group B1 sox genes. Development. 2009;136(15):2579–2589. 10.1242/dev.031344. [PubMed: 19570849]
60. Miranda CC, Fernandes TG, Pascoal JF, et al. Spatial and temporal control of cell aggregation efficiently directs human pluripotent stem cells towards neural commitment. Biotechnol J. 2015;10(10):1612–1624. 10.1002/biot.201400846. [PubMed: 25866360]
61. Koso H, Tsuhako A, Lai CY, et al. Conditional rod photoreceptor ablation reveals Sall1 as a microglial marker and regulator of microglial morphology in the retina. Glia. 2016;64(11):2005–2024. 10.1002/glia.23038. [PubMed: 27459098]
62. Yamada R, Mizutani-Koseki Y, Hasegawa T, Osumi N, Koseki H, Takahashi N. Cell-autonomous involvement of Mab21l1 is essential for lens placode development. Development. 2003;130(9):1759–1770. 10.1242/dev.00399. [PubMed: 12642482]
63. Fridman JS, Lowe SW. Control of apoptosis by p53. Oncogene. 2003;22(56):9030–9040. 10.1038/sj.onc.1207116. [PubMed: 14663481]
64. Riedl SJ, Salvesen GS. The apoptosome: signalling platform of cell death. Nat Rev Mol Cell Biol. 2007;8(5):405–413. 10.1038/nrm2153. [PubMed: 17377525]
65. Parker AL, Kavallaris M, McCarroll JA. Microtubules and their role in cellular stress in cancer. Front Oncol. 2014;4:153. 10.3389/fonc.2014.00153. [PubMed: 24995158]
66. Soond SM, Savvateeva LV, Makarov VA, Gorokhovets NV, Townsend PA, Zamyatnin AA Jr. Making connections: p53 and the Cathepsin proteases as co-regulators of cancer and apoptosis. Cancers (Basel). 2020;12(11). 10.3390/cancers12113476.
67. Nachmias B, Ashhab Y, Bucholtz V, et al. Caspase-mediated cleavage converts Livin from an antiapoptotic to a proapoptotic factor: implications for drug-resistant melanoma. Cancer Res. 2003;63(19):6340–6349. [PubMed: 14559822]
68. Dhuriya YK, Sharma D. Necroptosis: a regulated inflammatory mode of cell death. J Neuroinflammation. 2018;15(1):199. 10.1186/s12974-018-1235-0. [PubMed: 29980212]
69. Pasparakis M, Vandenabeele P. Necroptosis and its role in inflammation. Nature. 2015;517(7534):311–320. 10.1038/nature14191. [PubMed: 25592536]
70. Li J, Cao F, Yin HL, et al. Ferroptosis: past, present and future. Cell Death Dis. 2020;11(2):88. 10.1038/s41419-020-2298-2. [PubMed: 32015325]
71. Grasl-Kraupp B, Ruttkay-Nedecky B, Koudelka H, Bukowska K, Bursch W, Schulte-Hermann R. In situ detection of fragmented DNA (TUNEL assay) fails to discriminate among apoptosis, necrosis, and autolytic cell death: a cautionary note. Hepatology. 1995;21(5):1465–1468. 10.1002/hep.1840210534. [PubMed: 7737654]
72. Nguyen D, Yamada R, Yoshimitsu N, Oguri A, Kojima T, Takahashi N. Involvement of the Mab21l1 gene in calvarial osteogenesis. Differentiation. 2017;98:70–78. 10.1016/j.diff.2017.11.001. [PubMed: 29156428]
73. Gath N, Gross JM. Zebrafish mab21l2 mutants possess severe defects in optic cup morphogenesis, lens and cornea development. Dev Dyn. 2019;248(7):514–529. 10.1002/dvdy.44. [PubMed: 31037784]

74. Hartsock A, Lee C, Arnold V, Gross JM. In vivo analysis of hyaloid vasculature morphogenesis in zebrafish: a role for the lens in maturation and maintenance of the hyaloid. Dev Biol. 2014;394(2):327–339. 10.1016/j.ydbio.2014.07.024. [PubMed: 25127995]

75. Schlötzer-Schrehardt U, Zenkel M. The role of lysyl oxidase-like 1 (LOXL1) in exfoliation syndrome and glaucoma. Exp Eye Res. 2019;189:107818. 10.1016/j.exer.2019.107818. [PubMed: 31563608]

76. Thorleifsson G, Magnusson KP, Sulem P, et al. Common sequence variants in the LOXL1 gene confer susceptibility to exfoliation glaucoma. Science. 2007;317(5843):1397–1400. 10.1126/science.1146554. [PubMed: 17690259]

77. Wiggs JL, Pawlyk B, Connolly E, et al. Disruption of the blood-aqueous barrier and lens abnormalities in mice lacking lysyl oxidase-like 1 (LOXL1). Invest Ophthalmol Vis Sci. 2014;55(2):856–864. 10.1167/iovs.13-13033. [PubMed: 24425853]

78. Anderson MG, Meyer KJ, Hedberg-Buenz A, Fingert JH. Update on animal models of exfoliation syndrome. J Glaucoma. 2018;27(Suppl 1):S78–S82. 10.1097/IJG.0000000000000911. [PubMed: 29419647]

79. Zadravec P, Braunger BM, Melzer B, et al. Transgenic lysyl oxidase homolog 1 overexpression in the mouse eye results in the formation and release of protein aggregates. Exp Eye Res. 2019;179:115–124. 10.1016/j.exer.2018.11.001. [PubMed: 30399364]

80. Xia P, Wang S, Gao P, Gao G, Fan Z. DNA sensor cGAS-mediated immune recognition. Protein Cell. 2016;7(11):777–791. 10.1007/s13238-016-0320-3. [PubMed: 27696330]

81. Man SM, Karki R, Malireddi RK, et al. The transcription factor IRF1 and guanylate-binding proteins target activation of the AIM2 inflammasome by Francisella infection. Nat Immunol. 2015;16(5):467–475. 10.1038/ni.3118. [PubMed: 25774715]

82. Zhang X, Brann TW, Zhou M, et al. Cutting edge: Ku70 is a novel cytosolic DNA sensor that induces type III rather than type I IFN. J Immunol. 2011;186(8):4541–4545. 10.4049/jimmunol.1003389. [PubMed: 21398614]

83. Liu Y Semina EV. pitx2 deficiency results in abnormal ocular and craniofacial development in zebrafish. PLoS One. 2012;7(1):e30896. 10.1371/journal.pone.0030896. [PubMed: 22303467]

84. Kimmel CB, Ballard WW, Kimmel SR, Ullmann B, Schilling TF. Stages of embryonic development of the zebrafish. Dev Dyn. 1995;203(3):253–310. 10.1002/aja.1002030302. [PubMed: 8589427]

85. Gross-Thebing T, Paksa A, Raz E. Simultaneous high-resolution detection of multiple transcripts combined with localization of proteins in whole-mount embryos. BMC Biol. 2014;12:55. 10.1186/s12915-014-0055-7. [PubMed: 25124741]

86. Martin JA, Wang Z. Next-generation transcriptome assembly. Nat Rev Genet. 2011;12(10):671–682. 10.1038/nrg3068. [PubMed: 21897427]

87. Lin Y, Fine EJ, Zheng Z, et al. SAPTA: a new design tool for improving TALE nuclease activity. Nucleic Acids Res. 2014;42(6):e47. 10.1093/nar/gkt1363. [PubMed: 24442582]

88. Sanjana NE, Cong L, Zhou Y, Cunniff MM, Feng G, Zhang F. A transcription activator-like effector toolbox for genome engineering. Nat Protoc. 2012;7(1):171–192. 10.1038/nprot.2011.431. [PubMed: 22222791]

89. Meeker ND, Hutchinson SA, Ho L, Trede NS. Method for isolation of PCR-ready genomic DNA from zebrafish tissues. Bio-Techniques. 2007;43(5):610, 612, 614–614. 10.2144/000112619.

90. Erdmann B, Kirsch FP, Rathjen FG, More MI. N-cadherin is essential for retinal lamination in the zebrafish. Dev Dyn. 2003;226(3):570–577. 10.1002/dvdy.10266. [PubMed: 12619142]

91. Lu MF, Pressman C, Dyer R, Johnson RL, Martin JF. Function of Rieger syndrome gene in left-right asymmetry and craniofacial development. Nature. 1999;401(6750):276–278. 10.1038/45797. [PubMed: 10499585]

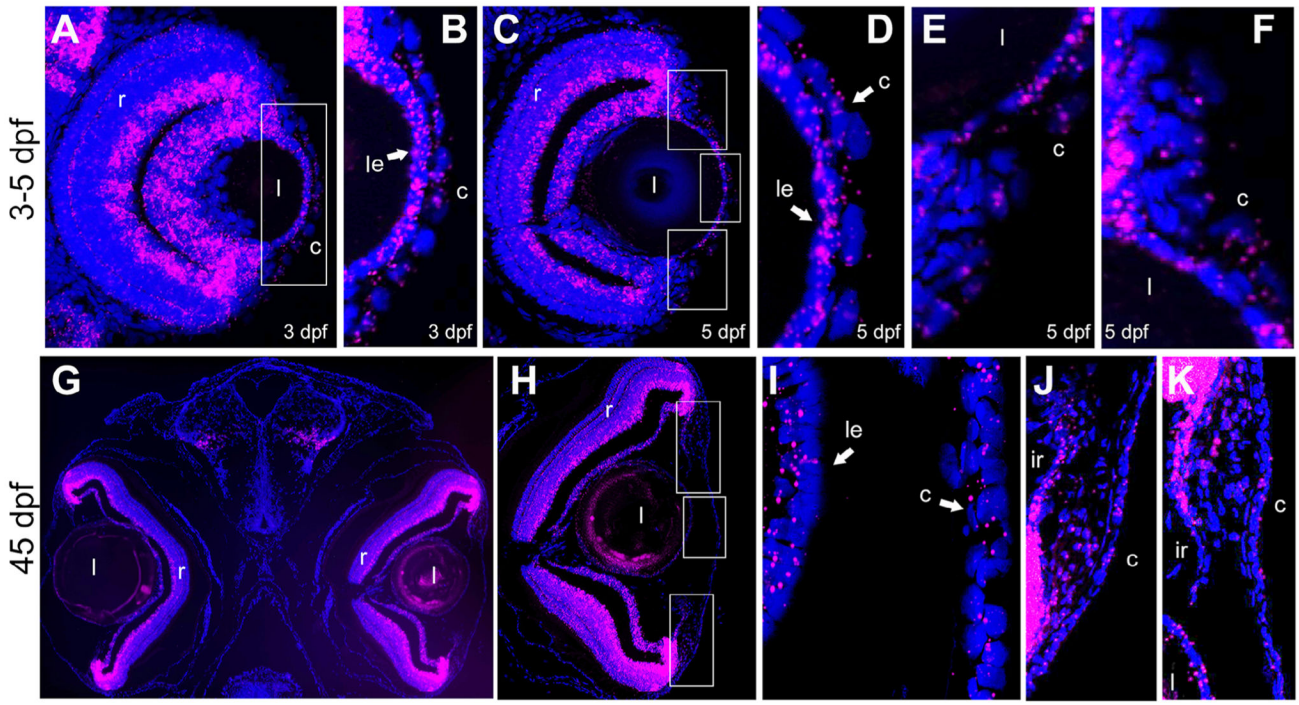

FIGURE 1.

Expression pattern of *mab21l1* in 3-, 5-, and 45-dpf zebrafish eye. RNA-scope analysis of *mab21l1* (magenta) in 3-dpf, A and B, 5-dpf, C-F, and 45-dpf, G-K, transverse sections. At all stages, *mab21l1* is expressed in the cornea (c) (both central, B, D, I, and peripheral, E, F, J, K), lens (l) (specifically, anterior lens epithelium [le]), and retina (r), A-K, as well as dorsal and ventral iris (ir) and iridocorneal angle at 45-dpf, J, K. DAPI staining indicates cell nuclei (blue). The boxed regions in, A, C, and H are shown in enlarged forms in, B, D-F, and I-K, respectively

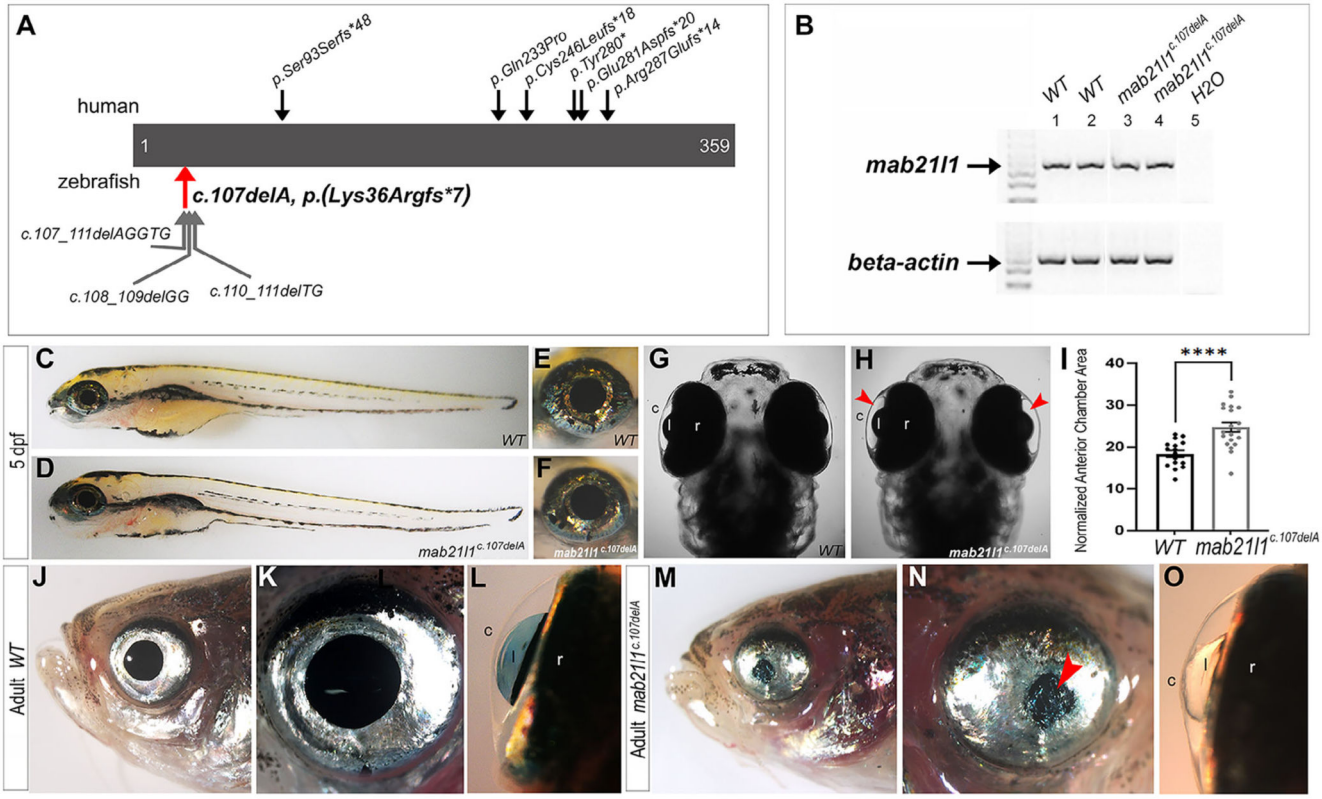

FIGURE 2.

MAB21L1/mab21l1 variants and gross phenotypic analysis of *mab21l1* deficient fish. A, Schematic of known human *MAB21L1* pathogenic variants (top) and zebrafish *mab21l1* alleles generated in this study (bottom). The red arrow indicates the zebrafish line chosen for detailed phenotypic characterization, *mab21l1-c.107delA* p.(Lys36Argfs*7). B, RT-PCR analysis of *mab21l1* transcript expression comparing 5-dpf wild-type (lanes 1 and 2) and homozygous *mab21l1-c.107delA* p.(Lys36Argfs*7) (lanes 3 and 4) embryos. Beta-Actin was used as a loading control. C-I, Assessment of 5-dpf phenotypes. No gross abnormalities between wild-type, C,E, and *mab21l1*$^{c.107delA}$ embryos, D,F, were detected in lateral position. However, an increase in anterior chamber area in *mab21l1*$^{c.107delA}$ embryos (G, H, indicated by red arrowheads in, H) was detected in dorsal view. This finding was quantified, I, and found to be statistically significant (**** $P = .0001$); error bars indicated SEM. J-O, Assessment of adult phenotypes (1–2 years of age). Smaller eyes with small/misshapen pupils, M, N, corneal opacities (N; red arrowhead), and irregularly shaped lens with keratolenticular adhesions, O, were observed. (c) cornea, (l) lens, (r) retina

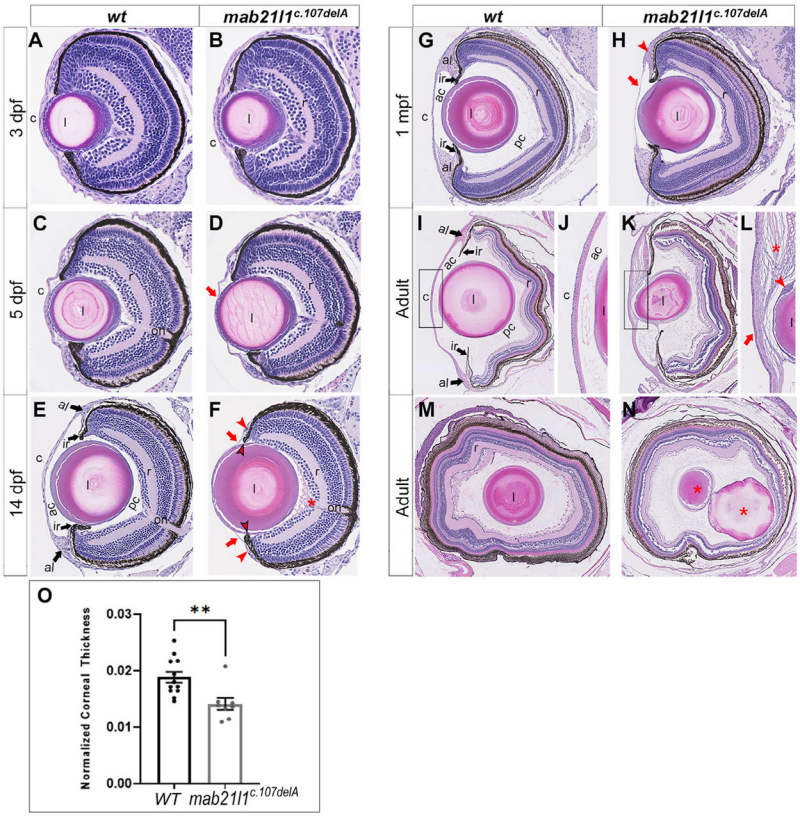

FIGURE 3.

Histological analysis of homozygous *mab21l1-c.107delA* p.(Lys36Argfs*7) ocular phenotypes. A-N. H&E stained transverse, A-L, and sagittal, M and N, sections of wild-type, A,C,E,G,I,J,M, and *mab21l1*$^{c.107delA}$ mutant, B,D,F,H,K,L,N, eyes at 3-dpf, A,B, 5-dpf, C,D, 14-dpf, E,F, 1-mpf, G,H, and adult (1–2 years), I-N, stages. No difference was observed at 3-dpf between wild-types and *mab21l1*$^{c.107delA}$, A and B. Beginning at 5-dpf and continuing at 14-hpf and 1-mpf, corneal thinning was observed in *mab21l1*$^{c.107delA}$ fish (D,F,H; indicated by red arrows). At 14-dpf, both the dorsal and ventral annular ligaments appear underdeveloped (indicated by red arrowhead), the dorsal and ventral iris appear short (red arrowhead outlined in black) and abnormal vasculature is present in the posterior segment (red asterisk) in *mab21l1*$^{c.107delA}$ mutants, F. At 1-mpf, the dorsal annular ligament remains underdeveloped (H, red arrowhead). In adult *mab21l1*$^{c.107delA}$ fish, K,L,N, abnormal corneal epithelium (red arrow) and fibrotic masses (K,L, red asterisk) in the anterior chamber, as well as abnormal lens epithelium (L, red arrowhead), small degenerative lenses, K-N, and abnormal lens material (N; red asterisks) were observed. (l) lens; (c) cornea; (r) retina; (ac) anterior chamber); (ir) iridocorneal region; (al) annular ligament; (pc) posterior chamber; (on) optic nerve. O, Measurements for total corneal thickness normalized to eye diameter for 5-dpf wild-type and mutants. Statistical significance is indicated by asterisks (** $P = .0048$); error bars indicate SEM

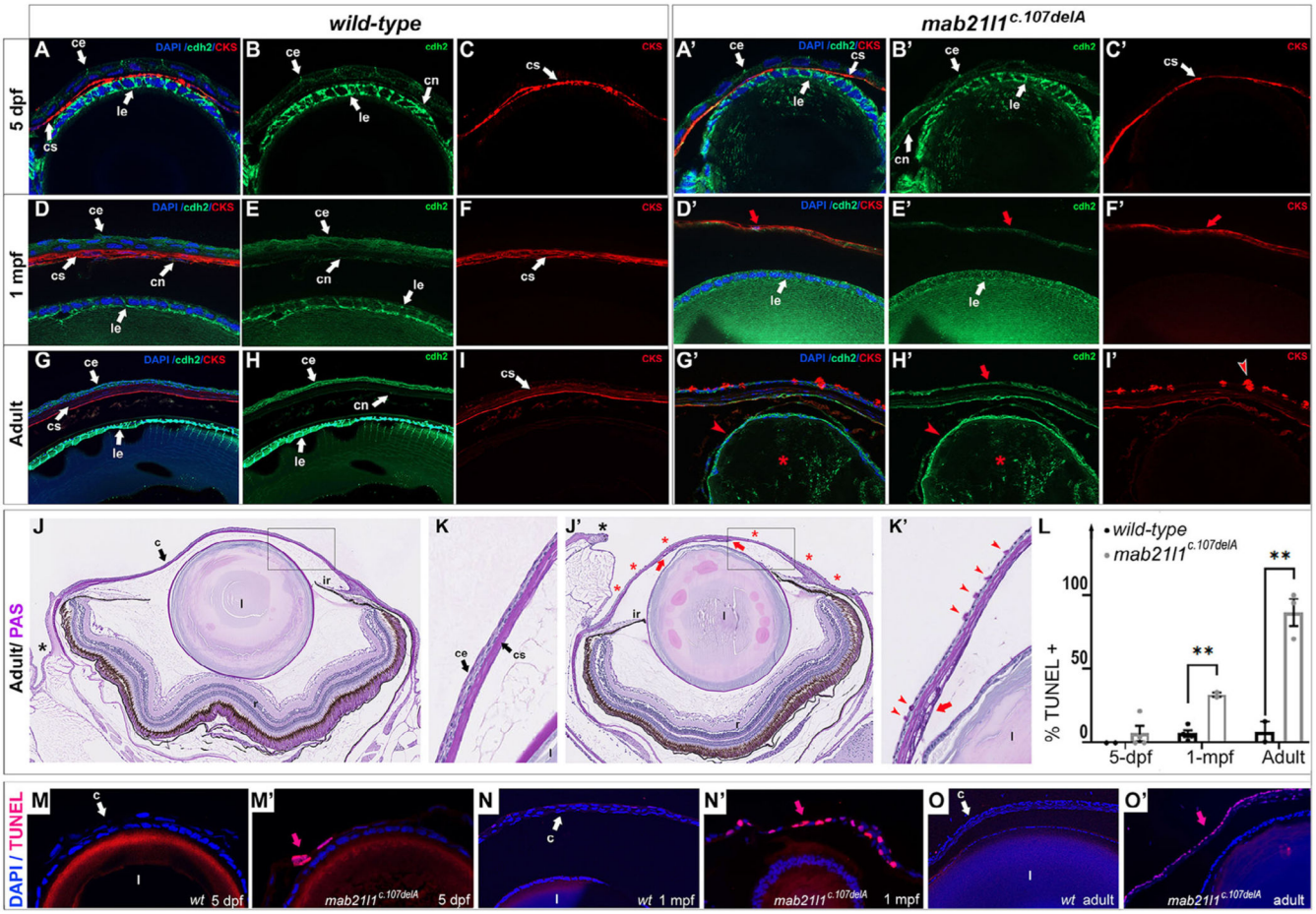

FIGURE 4.

Examination of the *mab21l1-c.107delA* p.(Lys36Argfs*7) ocular phenotype using immunohistochemistry, PAS staining and TUNEL fluorescence assays. A-I′, Wild-type, A-I, and *mab21l1*$^{c.107delA}$ mutant, A′-I′, transverse sections from 5-dpf, A-C, A′-C′), 1-mpf, D-F, D′-F′, and adults (1–2 years of age), G-I, G′-I′, were stained with DAPI (blue), cdh2 (green), and CKS (red). At 5-dpf, cdh2, and CKS staining highlights a thinner corneal epithelium (B′ vs. B) and stroma (C′ vs. C), correspondingly, observed in some *mab21l1*$^{c.107delA}$ embryos. At 1-mpf, thinning of the *mab21l1*$^{c.107delA}$ corneal epithelium (cdh2; E′ vs E) and stroma (CKS; F′ vs. F) becomes even more pronounced (red arrows in D′-F′). In *mab21l1*$^{c.107delA}$ adults, disorganized corneal layers with ectopic staining of CKS that can be detected throughout the outermost layer of the cornea (typically epithelium) are observed (I′ vs. I; red arrowhead in I′); additionally, lens degeneration is evident, highlighted by the absence of the cuboidal-shaped lens epithelial cells and disorganized cdh2 staining inside the lens (red arrowheads and asterisks in G′ and H′). (ce) corneal epithelium; (le) lens epithelium; (cs) corneal stroma; (cn) corneal endothelium. J-K′, Periodic acid-Schiff staining. Wild-type, J and K, and *mab21l1*$^{c.107delA}$ J′,K′, adults (1–2 years of age) transverse sections were PAS stained to visualize mucin-secreting goblet cells. In wild-type adults, PAS-stained mucin-secreting goblet cells are restricted to the peripheral ocular tissue (J, black asterisks), and cannot be detected within the central cornea (K inset). In

mab21l1$^{c.107delA}$ adults, PAS-stained goblet cells can be found at the ocular peripheries (J′, black asterisks), but can also be detected throughout the central cornea (J′ red asterisks, K′ inset red arrowheads). Red arrows in J′, K′ indicate abnormal corneal structures. (c) cornea; (l) lens; (r) retina, (ir) iridocorneal region; (ce) corneal epithelium; (cs) corneal stroma. L, Quantification of TUNEL assay. TUNEL positive cells were counted and percentage calculated to total DAPI-stained cells in cornea. Statistical significance is indicated by asterisks (1-mpf $^{**}P = .0021$; Adult $^{**}P = .0081$); error bars indicate SEM. M-O′. Representative images of TUNEL-stained wild-type, M,N,O, and *mab21l1*$^{c.107delA}$ mutant, M′, N′, O′, transverse sections at 5-dpf, M,M′, 1-mpf, N,N′, and adult, O, O′, eyes (red indicates dead cells). DAPI (blue) indicates cell nuclei. At all stages, an increase in TUNEL-stained cells was observed in *mab21l1*$^{c.107delA}$ mutant cornea (indicated by red arrows in, M′, N′ and O′, compared with wild-type. (c) cornea; (l) lens

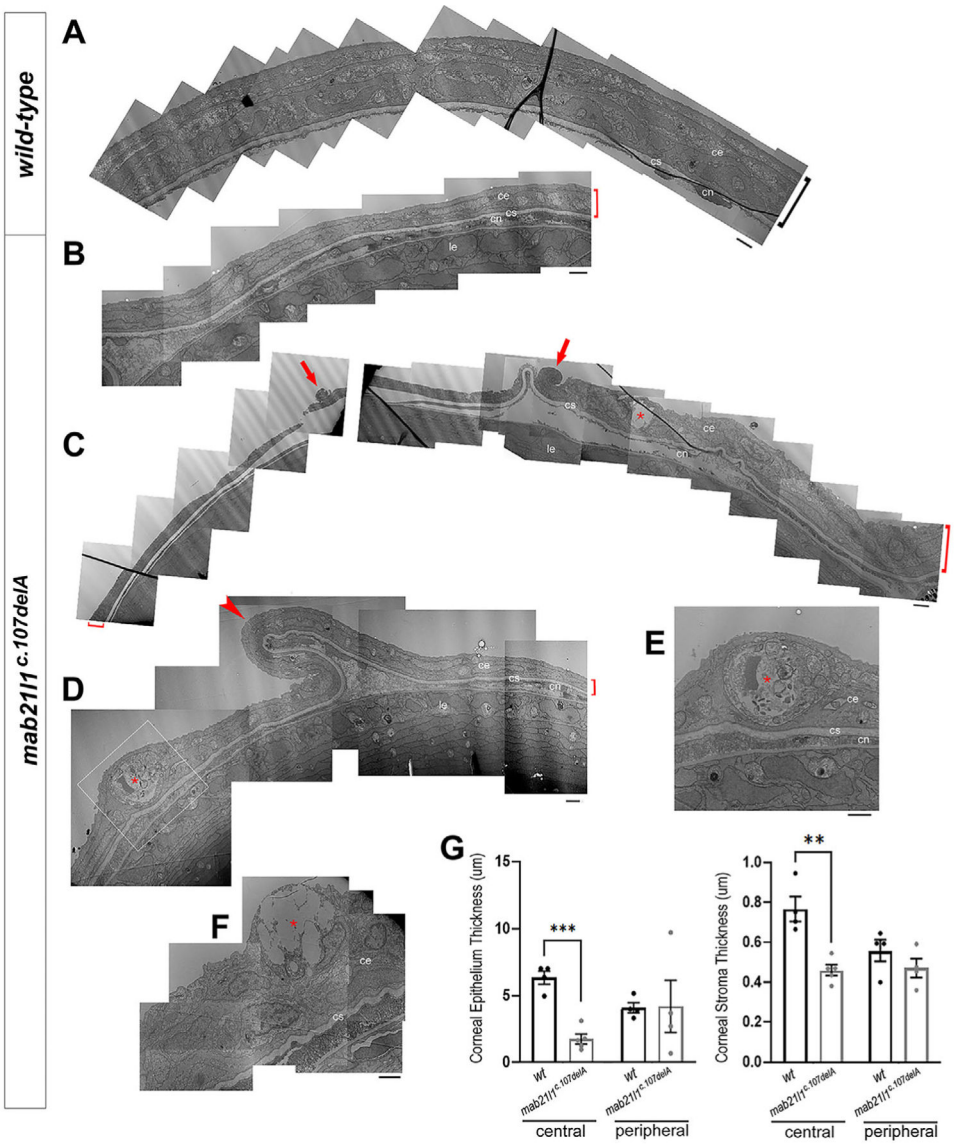

FIGURE 5.

Electron microscopy analysis of cornea. Electron microscopy data for 14-dpf wild-type, A, and *mab21l1*$^{c.107delA}$ mutant, B-F, corneas. Please note thinner (B,C,D; red brackets) and unevenly folded (D; red arrowhead) corneas, especially epithelial layer, in mutants vs wild-type, as well as the high number of abnormal cells (cells undergoing cell death [red arrows in, C], goblet [red asterisks in, C, F], and possible rodlet cells [red asterisks in D, E inset]); bar = 2 μM; (ce) corneal epithelium; (cs) corneal stroma; (cn) corneal endothelium; (le) lens epithelium. G, Measurements of corneal epithelial and stromal thickness for central and peripheral regions comparing wild-type and *mab21l1*$^{c.107delA}$ fish at 14-dpf based on EM images. Statistical significance is indicated by asterisks (central epithelium ***P = .00012; central stroma **P = .0018); error bars indicate SEM

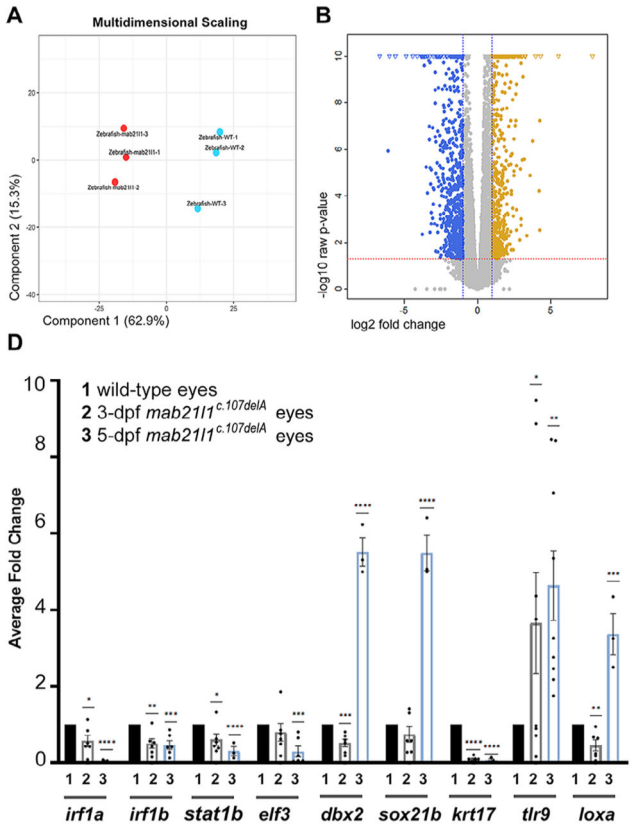

C

Zebrafish Gene Name	wild-type 1	wild-type 2	wild-type 3	mab21l1c.107delA 1	mab21l1c.107delA 2	mab21l1c.107delA 3	Human Homology	Fold Change
irf1a	1.61	0.90	-0.59	-0.59	-0.58	-0.75	*IRF1*	-11.27
LOC100538160	1.21	0.99	0.42	-1.02	-0.59	-1.00	*ZNF658*	-10.64
LOC110439587	1.52	0.59	0.25	-0.25	-1.06	-1.04	*ZNF723*	-5.88
LOC110437823	1.00	0.46	1.16	-1.11	-0.92	-0.61	*ZNF569*	-5.18
elf3	1.41	0.94	-0.34	-0.91	-1.10	0.00	*ELF3*	-4.60
stat1b	1.52	0.61	0.35	-0.78	-1.14	-0.55	*STAT1*	-4.28
pou3f3a	1.00	0.67	1.01	-1.06	-1.04	-0.58	*POU5F2*	-4.21
si:ch211-153b23.5	1.62	0.85	-0.77	-0.85	-0.44	-0.41	*HES1*	-3.95
krt17	0.94	0.95	0.83	-1.06	-0.73	-0.93	*KRT17*	-3.85
runx1	1.20	1.17	0.00	-0.36	-1.12	-0.90	*RUNX1*	-3.27
pax10	0.96	0.93	0.84	-0.95	-0.80	-0.98	*PAX6*	-3.22
irx4a	1.00	0.97	0.74	-0.77	-0.83	-1.11	*IRX4*	-3.14
LOC108183465	0.98	0.64	0.92	-0.51	-1.50	-0.53	*ZNF721*	-3.06
msx1a	0.57	1.70	-0.19	-0.36	-1.14	-0.57	*MSX1*	-3.03
loxa	-1.25	-1.03	0.01	1.42	0.44	0.41	*LOX*	2.14
LOC101887126	-1.12	-1.02	-0.46	0.97	1.17	0.46	*ZNF83*	3.02
sall1b	-1.20	-0.76	-0.74	0.85	1.00	0.84	*SALL1*	3.10
sox1a	-0.94	-0.97	-0.74	0.61	1.32	0.72	*SOX1*	3.25
LOC100537530	-0.60	-0.53	-0.62	1.96	-0.35	0.15	*ZNF569*	3.37
pou3f2b	-0.49	-1.26	-0.87	1.15	0.81	0.66	*POU3F2*	3.74
zgc:113135	-0.74	-0.79	-0.95	0.39	1.58	0.51	*ZNF568*	4.60
hsf4	-1.05	-0.86	-0.82	0.79	1.01	0.92	*HSF4*	5.02
sox21b	-0.85	-0.93	-0.92	0.75	1.22	0.71	*SOX21*	5.04
sall4	-0.81	-1.04	-0.88	0.77	0.98	0.97	*SALL4*	5.06
sox1b	-0.73	-1.04	-0.94	0.82	1.07	0.83	*SOX1*	5.20
prox2	-0.87	-1.10	-0.74	0.76	0.91	1.03	*PROX2*	5.40
her2	-0.86	-0.84	-1.01	1.00	0.69	1.03	*HES5*	5.58
helt	-0.71	-1.03	-0.87	0.46	0.81	1.34	*HELT*	8.19
tlr9	-0.83	-0.85	-0.83	0.97	1.39	0.14	*TLR9*	18.87
dbx2	-0.97	-0.74	-0.94	0.81	0.54	1.29	*DBX2*	19.60

FIGURE 6.

RNA seq data from wild type and *mab21l1* mutant embryos. A, Multidimensional Scaling Analysis. Multidimensional scaling (MDS) plot using the gene expression values of each sample. B, Volcano Plot of Expression Level of the up-regulated (yellow) and down-regulated (blue) transcripts. Log2 fold change and *P*-value obtained from the comparison between two groups plotted as volcano plot. (X-axis: log2 Fold Change, Y-axis: -log10 *P*-value). The dashed red line shows the *P*-value cutoff ($P = .01$) with points above the line having *P*-value <.01 and points below the line having *P*-value >.01. The vertical dashed blue lines show twofold changes. C, Heatmap for differentially expressed transcription factors and related genes. Zebrafish gene name and homologous human gene name are indicated, along with fold change. Gene names in red indicate transcripts validated by qRT-PCR. All transcripts except for *krt17, loxa* and *tlr9*, encode transcription factors (please see text). D, qRT-PCR analysis of select transcript (*irf1a, irf1b, stat1b, elf3, dbx2, sox21b, krt17, loxa*, and *tlr9*) level in RNA extracted from whole eyes of 3- and 5-dpf wild-type and *mab21l1*$^{c.107delA}$ embryos. The expression level in mutant embryos was normalized to wild-type expression at the same time-point. Bar graphs for 1, 2, and 3 indicate wild-type, 3-dpf *mab21l1*$^{c.107delA}$ and 5-dpf *mab21l1*$^{c.107delA}$, respectively. Statistical significance is indicated by asterisks; * $P \leq .05$, ** $P \leq .01$, *** $P \leq .001$, **** $P \leq .0001$; error bars indicate SEM